Bidirectional control of neurovascular coupling by cortical somatostatin interneurons

Boubacar Mohamed[1], Julie O'Reilly[1], Sandrine Picaud[1], Benjamin Le Gac[1], Esther Belzic[1], Liliana R V Castro[1], Hédi Soula[2], Isabelle Dusart[1], Dongdong Li[1], Bruno Cauli[1*]

1. Sorbonne Université, CNRS, INSERM, Neurosciences Paris Seine - Institut de Biologie Paris Seine (NPS-IBPS), 9 quai Saint Bernard, 75005 Paris, France.
2. Sorbonne Université, INSERM, Nutrition and Obesities: Systemic Approaches, NutriOmics, research unit, 91 boulevard de l'hôpital, 75013 Paris, France.

***Correspondence:** Bruno CAULI

9 Quai Saint Bernard, 75 005 Paris, France

Phone number: + 33 1 44 27 25 01

e-mail : bruno.cauli@upmc.fr

Running title: Control of neurovascular coupling by Sst neurons

Keywords: Neurovascular coupling, somatostatin interneurons, nitric oxide signaling, neuropeptide Y, optogenetics

ABSTRACT

Neurovascular coupling, linking neuronal activity to cerebral blood flow, is altered early in neurological disorders and underlies functional brain imaging. This process involves numerous cellular players. Among them inhibitory interneurons receive increasing attention, but how they control blood flow remains elusive. This study elucidates the mechanisms by which somatostatin interneurons bidirectionally control neurovascular coupling. Patch clamp recordings in, ex vivo, cortical slices from mice expressing channelrhodopsin-2 in somatostatin interneurons, revealed that these neurons are supralinearly activated at low-frequencies (< 5 Hz) and efficiently photostimulated at frequencies up to 20 Hz. Ex vivo vascular imaging showed that low-frequency (2 Hz) photostimulation triggered vasodilation whereas high-frequency (20 Hz) photostimulation induced vasoconstriction. Histochemistry revealed that subpopulations of cortical somatostatin interneurons expressed the neuronal nitric oxide synthase, and/or neuropeptide Y to a greater extent. Consistently, pharmacological investigations showed that vasodilation induced by low-frequency photostimulation involves nitric oxide release and activation of soluble guanylate cyclase. In contrast, the vasoconstriction induced at high-frequency photostimulation involves neuropeptide Y release and activation of the Y1 vascular receptor. These findings provide valuable insights into neurovascular coupling and help to understand the cellular mechanism underlying the functional brain imaging signals.

INTRODUCTION

Brain function and integrity are critically dependent on a permanent blood supply provided by a dense vascular network (Schaeffer and Iadecola, 2021). Cerebral blood flow (CBF) is also tightly controlled by neuronal activity, an essential process called neurovascular coupling (NVC) that is impaired in neurological disorders (Iadecola, 2017). The NVC is thought to ensure the optimal supply of metabolic needs to, and removal of waste products and heat from the activated brain regions, although its precise motive remains to be understood (Drew, 2022). It allows CBF to surge within seconds of increased neuronal activity and serves as the physiological basis for functional brain imaging techniques to map brain function (Iadecola, 2017). In the cerebral cortex, this hyperemic response is supported by dynamically controlled vasodilation that is spatially and temporally confined by vasoconstriction (Devor et al., 2007; Boorman et al., 2010; Uhlirova et al., 2016).

CBF is critically orchestrated by pial and penetrating arterioles, which have a higher density of contractile mural cells and control their diameter more rapidly than capillaries (Hill et al., 2015; Rungta et al., 2018; Hartmann et al., 2021). NVC is mediated by multiple vasoactive agents produced by excitatory neurons, astrocytes, GABAergic interneurons, and/or endothelial cells (Cauli and Hamel, 2018; Kaplan et al., 2020; Schaeffer and Iadecola, 2021) that control vessel diameter and CBF along the vascular tree (Rungta et al., 2018). These agents may be vasodilatory [e.g. arachidonic acid derivatives, nitric oxide (NO)], vasoconstrictive [e.g. Neuropeptide Y (NPY) (Uhlirova et al., 2016)], or both [e.g. glutamate, K^+ (Girouard et al., 2010; Zhang et al., 2024)].

The cellular diversity that characterizes cortical GABAergic interneurons (Ascoli et al., 2008), has made it challenging to study their contribution to NVC, and the conditions under which they release specific vasoactive agents have long remained elusive (Cauli et al., 2004). A major breakthrough in understanding their role came with the advent of transgenic mice and optogenetics, which allowed confirmation of their ability to induce vasodilation and/or vasoconstriction *in vivo* (Anenberg et al., 2015; Uhlirova et al., 2016). More recently the use of different Cre-line drivers has made it possible to investigate the contribution of different subpopulations of GABAergic interneurons (Krawchuk et al., 2019; Lee et al., 2020; Echagarruga et al., 2020; Krogsgaard et al., 2023; Ruff et al., 2024). Among these subclasses, somatostatin (Sst) interneurons have been found to either increase and/or decrease CBF

53 depending on the stimulation paradigm (Krawchuk et al., 2019; Lee et al., 2020), but the
54 underlying mechanisms of this bimodal response have not been determined.
55 To address this unresolved issue, we used *ex vivo* approaches in combination with
56 optogenetics to precisely control Sst interneurons firing in the mouse barrel cortex while
57 monitoring the resulting arteriolar response. We found that Sst interneurons are
58 supralinearly activated by low-frequency (< 5 Hz) photostimulation and are efficiently and
59 reliably activated up to 20 Hz. Low frequency stimulation (2 Hz) induced predominantly
60 vasodilation, whereas 20 Hz photostimulation resulted in vasoconstriction. Histochemical
61 analyses showed that subpopulations of Sst interneurons expressed the neuronal isoform of
62 NO synthase, NOS-1, and/or NPY at much greater extents. Pharmacological investigations
63 revealed that both types of vascular responses were dependent on action potential (AP)
64 firing. The vasodilation required NO synthesis and activation of the soluble guanylate cyclase
65 (sGC), whereas the vasoconstriction involved NPY and activation of its Y1 receptor. Thus, our
66 study elucidates the mechanisms by which Sst interneurons can induce vasodilation or
67 vasoconstriction depending on their firing frequency.
68

69 **MATERIALS AND METHODS**

70 **Animal models**

71 Homozygous Sst-IRES-Cre mice [Jackson Laboratory, B6J.Cg-*Sst*$^{tm2.1(cre)Zjh}$/MwarJ, stock#
72 028864, (Taniguchi et al., 2011)] were crossed with homozygous Ai32 mice [Jackson
73 Laboratory, B6.Cg-*Gt(ROSA)26Sor*$^{tm32(CAG-COP4*H134R/EYFP)Hze}$/J stock #024109,
74 (Madisen et al., 2012)] or with homozygous Ai95d mice [Jackson Laboratory, B6J.Cg-
75 *Gt(ROSA)26Sor*$^{tm95.1(CAG-GCaMP6f)Hze}$/MwarJ, stock# 028865 (Madisen et al., 2015)], to
76 obtain heterozygous Sst$^{Cre/WT}$::Ai32$^{ChR2/WT}$ (Sst-ChR2) for optogenetic stimulations or
77 Sst$^{Cre/Wt}$::Ai95d$^{GCaMP6f/Wt}$ (Sst-GCaMP6f) mice for immunohistochemistry. C57BL/6RJ mice
78 were used for control optogenetic experiments and exogenous NPY applications. 16-21 days
79 postnatal old females and males were used for all experiments. All experimental procedures
80 involving animals were carried out in strict compliance with French regulations (Code Rural
81 R214/87 to R214/130) and in accordance with the ethical guidelines of the Directive of the
82 Council of the European Communities of September 22, 2010 (2010/63/EU).
83

84 ***Ex vivo* slice preparation**

85 Mice were deeply anesthetized by isoflurane (IsoVet Piramal Healthcare UK or IsoFlo,
86 Axience) evaporation in an induction box then euthanized by decapitation. The brain was
87 quickly removed and immersed in cold (~ 4°C) oxygenated artificial cerebrospinal fluid (aCSF)
88 containing in (mM): 125 NaCl, 2.5 KCl, 1.25 NaH_2PO_4, 2 $CaCl_2$, 1 $MgCl_2$, 26 $NaHCO_3$, 10
89 glucose, 15 sucrose and 1 kynurenic acid (Sigma-Aldrich). 300 µm-thick coronal slices
90 containing the barrel cortex were cut with a vibratome (VT1000s; Leica) and were allowed to
91 recover at room temperature for at least 45 min with oxygenated aCSF (95% O_2/5% CO_2)
92 (Devienne et al., 2018). The slices were transferred to a recording chamber and continuously
93 perfused at a rate of ~2 ml/min with oxygenated aCSF lacking kynurenic acid.

94

95 **Patch-clamp recording**

96 Borosilicate glass patch pipettes (5.0 ± 0.4 MΩ) were filled with an internal solution
97 containing (in mM): 144 K-gluconate, 3 $MgCl_2$, 0.5 EGTA, 10 HEPES, pH 7.2 (285/295 mOsm).
98 Sst-ChR2 interneurons were first visually identified by their EYFP fluorescence. Whole-cell
99 recordings were performed at room temperature (20-25 °C) using a patch clamp amplifier
100 (Axopatch 200B, Molecular Devices) at a wavelength of 780 nm, which does not activate
101 ChR2 (Lin et al., 2009). Data were filtered at 5-10 kHz and digitized at 50 kHz using an
102 acquisition board (Digidata 1440, MDS) attached to a personal computer running pCLAMP
103 10.7 software package (MDS). Electrophysiological properties were determined using the
104 fast I-clamp mode of the amplifier and were measured as previously described (Karagiannis
105 et al., 2021, 2009). Membrane potential values were not corrected for liquid junction
106 potential. Only neurons with a resting membrane potential more hyperpolarized than -55
107 mV were further analyzed.

108

109 **Optogenetic stimulation**

110 Optogenetic stimulation performed through the objective using a 470 nm light-emitting
111 diode (LED) device (CoolLED brand, Precise Excite model) attached to the epifluorescence
112 port of a BX51WI microscope (Olympus) and a set of multiband filters consisting of an
113 excitation filter (HC 392/474/554/635, Semrock), a dichroic mirror (BS 409/493/573/652,
114 Semrock), and an emission filter (HC 432/515/595/730, Semrock). Photostimulation

115 consisted of a 10-s train of 5 ms light pulses at an intensity of 38 mW/mm² and delivered at
116 six different frequencies (1, 2, 5, 10, 20 and 40 Hz).

117 **Vascular imaging**

118 Blood vessels and cells were observed in slices under infrared illumination with Dodt
119 gradient contrast optics (IR-DGC Luigs and Neumann; (Dodt and Zieglgansberger, 1998))
120 using a collimated LED (780 nm; ThorLabs) as the transmitted light source, a 40X
121 (LUMPlanF/IR, 40X/0.80 W, Olympus) and a digital camera (OrcaFlash 4.0LT+, Hamamatsu)
122 attached to the microscope. Diving arterioles were selected by IR-DGC based on their well-
123 defined luminal diameter (16.7 ± 0.5 µm, n = 144 arterioles), their length remaining in the
124 focal plane of at least 50 µm, and the thickness of their wall (5.5 ± 0.1 µm, n = 144
125 arterioles). A resting period of at least 30 min (Lovick et al., 1999; Zonta et al., 2003) was
126 observed after slice transfer. IR-DGC images were acquired at 0.1 Hz for pharmacological
127 applications and at 1 Hz for optogenetic experiments using Imaging Workbench 6.1 software
128 (Indec Biosystems). The focal plane was continuously maintained on-line using IR-DGC
129 images of cells as anatomical landmark (Lacroix et al., 2015). After light-induced responses,
130 arteriolar identity and reactivity were systematically verified by assessing their contractility
131 (Hartmann et al., 2021) using the thromboxane A2 analog, U46619 (100 nM) (Cauli et al.,
132 2004; Rancillac et al., 2006). Blood vessels that failed to constrict after this pharmacological
133 application were discarded. Only one arteriole was monitored per slice.

134

135 **Double fluorescence immunolabeling**

136 Mice were euthanized with pentobarbital (150 mg/kg, i.p., Euthasol Vet) and their brains
137 were perfusion fixed (50 ml of ice-cold 4 % paraformaldehyde (PFA), in 0.1M phosphate
138 buffer, pH 7.4), and post-fixed by immersion in 4 % PFA (2 h, 4°C). Brains were then cut in 50
139 µm-thick coronal sections with a VT-1000S vibratome (Leica). After washing in PBS, free-
140 floating sections were blocked for 2 h at room temperature in a PBS 1X/0.25% Triton X-
141 100/0,2% gelatin solution before being incubated overnight at 4°C with primary antibodies.
142 Sections from 3 to 4 different mouse brains were simultaneously incubated overnight with
143 the primary antibodies against GFP and specific markers. Antibodies included chicken anti-
144 GFP (1:1000; Aves Labs GFP-1020, (Tricoire et al., 2010)), rabbit anti-NOS-1 (1:1000,
145 Millipore AB5380, (Tricoire et al., 2010)), sheep anti-NPY (1:2000, Abcam ab6173, (Lee et al.,
146 2010)). The respective immunoreactions were visualized with the following secondary

147 antibodies: goat anti-chicken Alexafluor 488 (1:1000, Invitrogen A11039), donkey anti-rabbit
148 Alexafluor 555 (1:1000, Invitrogen A31572) donkey anti-sheep Alexafluor 555 (1:1000,
149 Invitrogen A21436). Nuclear counterstaining was performed with 100 ng/ml DAPI (4',6-
150 diamidino-2-phenylindole; Invitrogen) solution in PBS for 20 min. Sections were mounted
151 with Fluoromount G (SouthernBiotech) on gelatin-coated slides for visualization. Images of
152 immunostained material were acquired and processed in Airyscan 2 mode using a LSM 980
153 confocal microscope with a 20x objective (N Plan-Apochromat 20x) and ZEN Blue 3 software
154 (Zeiss). Cell counting was achieved using the cell counter plug-in of FIJI software.
155
156 **Drugs**
157 All pharmacological compounds were bath-applied after a 5-minute control period (aCSF)
158 and vascular dynamics were recorded during bath application. The following drugs were
159 dissolved in water: NPY (Enzo, ALX-163-003), Nω-Nitro-L-arginine methyl ester hydrochloride
160 (L-NAME, Sigma-Aldrich, N5751), BIBP3226 (1 µM, Tocris, 2707). Tetrodotoxin (TTX, 1 µM,
161 Latoxan, L8503) was dissolved in 90% acetic acid. 1H-[1,2,4] oxadiazolo[4,3-a]quinoxalin-1-
162 one (ODQ, Sigma-Aldrich, O3636) was dissolved in DMSO and 9,11-dideoxy-9α,11α-
163 methanoepoxy prostaglandin F2α (U-46619, 100 nM, Enzo, BML-PG023) in ethanol. Acetic
164 acid, DMSO and ethanol doses were always used below 0.1% to avoid vascular interactions
165 (Sun et al., 2010). NO pathway inhibitors, BIBP3226 and TTX were applied at least 30 min
166 before optogenetic stimulation or exogenous NPY application.
167
168 **Vascular reactivity analysis**
169 To compensate for potential x-y drifts, all images were realigned off-line using the
170 "StackReg" plug-in (Thevenaz et al., 1998) of the ImageJ 1.54f software. Luminal diameter
171 was measured on registered images using custom analysis software developed in MATLAB
172 (MathWorks) (Lacroix et al., 2015). Only arterioles with a stable luminal diameter were
173 analyzed further. Arterioles were considered stable if the relative standard deviation (RSD)
174 of their luminal diameter during the baseline period was less than 5% (Lacroix et al., 2015).
175 The impact of blockers, inhibitors, and antagonists on arterioles was evaluated by comparing
176 the mean luminal diameter during the initial 5 minutes of the baseline period and the final 5
177 minutes of the treatment period prior to optogenetic stimulation or NPY application.
178 Diameter changes ($\Delta D/D_0$) were expressed according to: $(Dt - D_0)/D_0$ where Dt is the luminal

179 diameter at the time t and D_0 the average diameter during the 5 minutes baseline period.
180 Vasomotor responses and their parameters were determined from the diameter change
181 traces [$\Delta D/D_0 = f(t)$] plotted using Clampfit 10.7 (MDS). To determine whether arterioles
182 dilated or constricted, a Z-score was calculated from the diameter change traces using the
183 formula: $Z = (x - \mu)/ \sigma$, where both the mean μ and standard deviation σ were calculated
184 using the values before photostimulation or NPY application. Vascular responses were
185 classified as vasodilation or vasoconstriction, respectively, if the Z-score exceeded a value of
186 1.96 (95% criteria) or fell below -1.96 for 10 seconds and 1 minute for photostimulation and
187 NPY application, respectively. For each vascular response, the time of onset and peak
188 (relative to the beginning of stimulation), duration, maximal amplitude and magnitude (area
189 under the curve [AUC]) were determined (Supplementary Fig. 2). When multiple events of
190 vasodilation or vasoconstriction occurred, the earliest onset was used for global onset, the
191 time and amplitude of the largest maximum amplitude were used for global time to peak
192 and global maximum amplitude, and the sum of durations and magnitudes was used for
193 global duration and magnitude.
194
195 **Statistical analyses**
196 Statistical analyses were performed using GraphPad Prism version 8.0.2 (GraphPad Software,
197 La Jolla, California, USA). All values are expressed as means ± SEM. Normality of distribution
198 was assessed using the Shapiro-Wilk test. Parametric tests were only used if this criterion
199 was met. The mean spike success rate per light pulse between photostimulation frequencies
200 was compared using the Q Friedman test. Comparisons of vascular responses were
201 determined using Brown-Forsythe ANOVA or Kruskal-Wallis tests. Given p-values were
202 corrected for multiple comparisons using the original False Discovery Rate method of
203 Benjamini and Hochberg (Benjamini and Hochberg, 1995). Statistical significance on all
204 figures uses the following convention: $*p < 0.05$, $**p < 0.01$ and $***p < 0.001$.
205

206 **RESULTS**

207 **Sst interneurons are efficiently activated by optogenetic stimulation over a wide range of**
208 **frequencies.**

209 To evaluate the frequency dependence of the vascular response driven by Sst interneurons,
210 we optogenetically elicited their AP firing while visualizing the evoked vascular response in
211 cortical brain slices from $Sst^{Cre/WT}$::$Ai32^{ChR2/WT}$ mice (Madisen et al., 2012; Taniguchi et al.,
212 2011) conditionally expressing the H134R variant of channelrhodopsin-2 (ChR2) in Sst
213 interneurons. We first determined the electrophysiological phenotype of Sst-ChR2 cortical
214 neurons using whole-cell patch clamp recordings. Cortical neurons expressing EYFP/ChR2
215 were selected based on their EYFP fluorescence (Fig. 1a and Supplementary Fig. 1) in layers
216 II-III (n=13 neurons) and V (n=3 neurons). Most neurons exhibited electrophysiological
217 features typical of adapting-Sst interneurons (Karagiannis et al., 2009, 2021; Perrenoud et
218 al., 2012a), including a relatively high membrane resistance (608 ± 231 MΩ) and a
219 pronounced voltage sag (21.2 ± 10.8 %) in response to hyperpolarizing current pulses (Fig.
220 1a, middle traces). They also exhibited a low rheobasic current (8 ± 14 pA, Fig. 1a) and a
221 slowly developing early frequency adaptation (adaptation time constant: 60.5 ± 23.8 ms)
222 when depolarized by high stimulation intensities (Fig. 1a). Consistently, the
223 hyperpolarization (AHP) phase of their action potentials consisted of a fast AHP, followed by
224 an afterdepolarization (ADP) and a medium AHP (Fig. 1a and Supplementary Table 1).
225 However, as previously reported in Sst-Cre cortical neurons (Hu et al., 2013) and expected
226 from the occasional expression of Sst transcripts in parvalbumin neurons (Cauli et al., 1997;
227 Tasic et al., 2016), one Sst-ChR2 neuron exhibited the electrophysiological features of a fast
228 spiking cell with a low input resistance (129 MΩ), a fast time constant (11.7 ms), a high
229 rheobase (185 pA), short spikes (0.6 ms) with a sharp fast AHP (-26.5 mV), and the ability to
230 fire high firing rates (maximal frequency: 99 Hz) with little frequency adaptation
231 (Supplementary Fig. 1 and Table 1).

232 Next, we evaluated the efficiency of optogenetic stimulation by recording the voltage
233 response of the patched Sst-ChR2 neurons. Wide-field photostimulation was achieved using
234 10-second trains of 5 ms light pulses (see Materials and Methods) delivered at six different
235 frequencies (1, 2, 5, 10, 20 and 40 Hz, Fig. 1b, lower traces). Surprisingly, at the beginning of
236 the light pulse trains, Sst-ChR2 neurons fired up to five APs per light pulse (Fig. 1b, upper
237 traces). Such bursting response declined within seconds before reaching a steady state level

238 (Fig. 1b, middle traces). The instantaneous spike success rate remained above 100 % at
239 stimulation frequencies below 10 Hz, while it decreased below 100% at higher frequencies
240 (Fig. 1b, middle traces). Consistent with the kinetic properties of the H134R ChR2 variant (Lin
241 et al., 2009), Sst-ChR2 neurons were not able to sustain the firing of action potentials when
242 photostimulated at 40 Hz (Fig. 1b6). The mean spike success rate over the 10 s train differed
243 between photostimulation frequencies (Fig. 1c, $Q_{(6,9)}$= 41.89, p= 6.203 10^{-8}, 1 Hz: 176 ± 13%;
244 2 Hz: 197 ± 15%; 5 Hz: 118 ± 11%; 10 Hz: 103 ± 10%; 20 Hz: 97 ± 5%; 40 Hz: 25 ± 7%, n=9 Sst-
245 ChR2 neurons). Indeed, photostimulation at 1 Hz and 2 Hz showed a higher number of APs
246 per light pulse than that observed at frequencies above 5 Hz (Fig. 1c, 1Hz vs. 10 Hz, p=
247 0.0374; 1Hz vs. 20 Hz, p= 0.0063; 1 Hz vs. 40 Hz, p= 7.000 10^{-6}; 2 Hz vs. 10 Hz, p = 0.0245; 2Hz
248 vs. 20 Hz, p= 0.0039, 2 Hz vs. 40 Hz, p=3.597 10^{-6}). Taken together, these observations
249 indicate that optogenetic stimulation efficiently and reliably activates Sst-ChR2 neurons,
250 mostly of the adapting Sst subtype, at frequencies up to 20 Hz. They also reveal that these
251 neurons over-respond to low frequencies of photostimulation.
252
253 **The polarity of the vascular response induced by the optogenetic stimulation of Sst-ChR2**
254 **neurons is frequency dependent.**
255 Next, we visualized the optogenetically induced response of diving arterioles in cortical slices
256 (Fig. 2). We focused on the photostimulations at 2 Hz and 20 Hz, which correspond
257 respectively to the highest AP number per light pulse and to the frequency that produced
258 the highest total AP number, respectively (Fig. 1b,c). When photostimulation was delivered
259 at 2 Hz in Sst-ChR2 slices, we observed that the vast majority of arterioles exhibited
260 vasodilatory events (n= 13 of 14 arterioles, Fig. 2a,b), which could be accompanied by
261 vasoconstrictive events (n=6 of 14). On average, this resulted in a slight vasodilation (Fig. 2c).
262 High light intensity can cause dilation (Rungta et al., 2017) or constriction (Choi et al., 2010)
263 independent of ChR2, so we did control experiments by repeating 2 Hz photostimulation in
264 slices of C57Bl6 mice that do not express ChR2 (Fig. 2c). Although the overall vascular
265 response, as estimated by the area under the curve (AUC) of the response following the
266 optogenetic stimulation did not differ between Sst-ChR2 (55.8 ± 24.1 %.min, n= 14
267 arterioles) and C57Bl6 arterioles (37.4 ± 15.3 %.min, n= 6 arterioles, p= 0.15146, Fig. 2g1), an
268 evident tendency was observed toward vasodilation in Sst-ChR2 arterioles (Fig. 2c). Because
269 both vasodilation and vasoconstriction can occur in the same arteriole (Fig. 2b), we refined

270 the analysis of vascular responses by separating vasodilatory events from vasoconstrictive
271 events based on a Z-score test (supplementary Fig. 2a-b, see Methods). The magnitude of
272 vasodilation was greater in Sst-ChR2 arterioles (69.6 ± 19.9 %.min, Fig. 2g2) than in control
273 arterioles (8.5 ± 4.5 %.min, p=0.03415), although not the maximal amplitude (Sst-ChR2: 6.1 ±
274 1.3 % *vs.* C57Bl6: 2.2 ± 0.7 %, p= 0.12763, Fig. 2g3). Vasodilation also occurred earlier and
275 lasted longer in Sst-ChR2 arterioles (onset: 221 ± 130 s, duration: 1121 ± 195 s) than in
276 control arterioles (onset: 1013 ± 314 s, p= 0.02501, Fig. 2g4, duration: 304 ± 135 s, p=
277 0.04865, Fig. 2g6) but did not differ in their time to peak (Sst-ChR2: 669 ± 155 s *vs.* C57Bl6:
278 1014 ± 314 s, p= 0.32174, Fig. 2g5). In contrast, the amplitude, magnitude, and kinetic
279 properties of vasoconstriction induced by photostimulation at 2 Hz did not differ between
280 Sst-ChR2 and C57Bl6 arterioles (supplementary Fig. 2c1-5).
281 We next evaluated whether a stronger optogenetic stimulation could induce a similar
282 vascular response. Surprisingly, photostimulation at 20 Hz of Sst-ChR2 slices (n= 16) induced
283 vasoconstrictive events in the vast majority of arterioles (n= 15 of 16), but also vasodilatory
284 events to a lesser extent (n=9 of 16, Fig. 2d,e). This resulted on average in a progressive
285 vasoconstriction that was not observed in control arterioles (n= 4, Fig. 2f). Although the
286 overall vascular response was not statistically different between Sst-ChR2 and C57Bl6
287 arterioles (p=0.13458, Fig. 2h1), similarly to 2 Hz photostimulation it was more
288 heterogeneous in Sst-ChR2 arterioles (-83.3 ± 46.7 %.min) than in C57Bl6 arterioles (0.0 ±
289 25.3 %.min) and may be associated with both vasoconstriction and vasodilation (Fig. 2d,e
290 and supplemental Fig. 2 a,b). Both the magnitude of vasoconstriction and the maximal
291 vasoconstriction were greater in Sst-ChR2 arterioles (AUC: -121.7 ± 35.4 %.min, Fig. 2h2;
292 Maximal constriction: -12.2 ± 2.7 %, Fig. 2h3) than in control C57Bl6 (AUC: -17.8 ± 17.8
293 %.min, p=0.01810; Maximal constriction: -1.6 ± 1.6 %, p=0.00505). The onset and time to
294 peak of vasoconstriction were also earlier in Sst-ChR2 arterioles (onset: 267 ± 120 s, Fig. 2h4;
295 time to peak: 874 ± 181 s, Fig. 2h5) compared to control C57Bl6 arterioles (onset: 1361 ± 439
296 s; p= 0.01993; time to peak: 1680 ± 121 s, p= 0.04397). The contraction duration did not
297 differ between Sst-ChR2 arterioles (981 ± 152 s) and C57Bl6 (424 ± 424 s, p= 0.13849, Fig.
298 2h6). In contrast, the amplitude, magnitude, and kinetic properties of vasodilatory events
299 induced by photostimulation at 20 Hz did not differ between Sst-ChR2 and C57Bl6 arterioles
300 (supplementary Fig. 2d1-5). Taken together, these observations indicate that, depending on
301 the frequency of optogenetic stimulation Sst-ChR2 neurons elicit a bidirectional vascular

302 response consisting mainly of vasodilation and vasoconstriction at 2 Hz and at 20 Hz,
303 respectively.

304 **NOS-1 and NPY are expressed by subpopulations of Sst cortical interneurons**

305 Subpopulation of Sst-expressing cortical interneurons have been reported to produce NO
306 and/or NPY (Hendry et al., 1984; Kubota et al., 1994, 2011; Perrenoud et al., 2012a). These
307 mediators may explain the bidirectional vascular responses induced by the photostimulation
308 of Sst-ChR2 interneurons at 2 and 20 Hz, respectively, as they have been shown to induce
309 vasodilation and vasoconstriction, respectively (Cauli et al., 2004; Rancillac et al., 2006). We
310 therefore used double immunohistofluorescence to determine the extent to which Sst
311 interneurons have the ability to produce NO and NPY. Consistent with previous reports
312 (Kubota et al., 1994, 2011; Perrenoud et al., 2012a), NOS-1 immunolabeling revealed that
313 strongly immunoreactive somata appeared denser in deep than in superficial cortical layers
314 (Fig. 3a2-3 and supplementary Fig. 3). Some of these neurons were clearly identified as Sst-
315 ChR2 interneurons as shown by immunolabelling of the ChR2-EYFP fusion transgene using an
316 anti-GFP antibody (supplementary Fig. 3). However, consistent with the membrane
317 localization of ChR2-EYFP (Fig. 1a and supplementary Fig. 1), GFP immunofluorescence was
318 present at the periphery of the somata and in a dense fiber plexus (supplementary Fig. 3)
319 making it difficult to evaluate the degree of co-expression. Therefore, we thus used Sst-
320 GCamp6 mice (n= 3 mice) to obtain somatic Cre-dependent expression of the circularly
321 permuted GFP of GCamp6 (Madisen et al., 2015). As previously reported in Sst-IRES-Cre mice
322 (Taniguchi et al., 2011), Cre-dependent GFP expression was observed in the somata of
323 neurons distributed throughout all cortical layers except layer I (Fig. 3a1,b1), which
324 nevertheless showed diffuse GFP labelling presumably originating from the ascending axon
325 of Martinotti cells branching in this layer (DeFelipe et al., 2013). The average density of GFP-
326 positive cells was comparable between sections immunostained for NOS-1 (49.9 ± 2.7
327 cells/mm^2, n=3 mice, Fig. 3a1) and NPY (41.0 ± 7.1 cells/mm^2, n= 3 mice, Fig. 3b1,
328 t(2.55619)= 1.16763, p= 0.3403). A similar density of neurons immunolabeled for NOS-1 was
329 observed in GFP positive (2.0 ± 0.1 cells/mm^2) and negative cells (1.9 ± 0.4 cells/mm^2,
330 t(2.28582)= 0.215387, p= 0.8472, Fig. 3a3-4). However, the intensity of NOS-1
331 immunostaining was stronger in GFP-positive cells than in negative cells (Fig. 3a1,2),
332 indicating that they likely correspond to type 1 and type 2 NO-producing interneurons,
333 respectively. Consistent with previous reports in Sst interneurons, (Kubota et al., 1994, 2011;

334 Karagiannis et al., 2009; Perrenoud et al., 2012a; Tricoire et al., 2013), putative type 1 NO
335 interneurons represented only a minority of GFP-positive cells (4.0 ± 0.1%). NPY
336 immunostaining showed a relatively high density of positive cells (29.4 ± 6.0 cells/mm^2) and
337 fiber plexus in superficial and deep layers (Fig. 3b2) as reported in other mammals (Hendry
338 et al., 1984). The vast majority of NPY immunoreactive neurons were also GFP positive (81.4
339 ± 2.1%, Fig. 3b3-4) with the remaining NPY interneurons likely corresponding to
340 neurogliaform cells (Cauli et al., 2004; Price et al., 2005; Karagiannis et al., 2009; Kubota et
341 al., 2011; Perrenoud et al., 2012a), as suggested by their round immunolabeled somata (Fig.
342 3b3-4). More precisely, the proportion of GFP-positive cells immunostained for NPY was
343 much higher (58.9 + 8.2%, t(2.00020)=6.70695, p= 0.0215) than those immunolabeled for
344 NOS-1, which is known to represent a subpopulation of NPY interneurons (Estrada and
345 DeFelipe, 1998; Karagiannis et al., 2009; Tasic et al., 2016). These observations collectively
346 indicate that the Cre-dependent expression of the transgenes in Sst-IRES-Cre mice occurs in
347 at least two subpopulations of interneurons that express NOS-1 and/or NPY to a greater
348 extent.
349
350 **Vasodilation induced by 2 Hz photostimulation of Sst-ChR2 interneurons requires AP firing**
351 **and NO signaling**
352 Since a subpopulation of Sst interneurons (Fig. 3a3-4 and supplementary 3) can produce the
353 vasodilator NO (Cauli et al., 2004), we next investigated the mechanisms by which they
354 induce vasodilation when photostimulated at 2 Hz. We first determined whether spiking
355 activity was required by blocking APs with the voltage-activated sodium channel blocker
356 tetrodotoxin (TTX 1 µM (Zonta et al., 2003), n= 10 arterioles). Bath application of TTX did not
357 change arteriolar diameter (diameter before: 17.0 ± 1.8 µm *vs.* after TTX: 16.9 ± 1.7 µm, $t_{(9)}$=
358 1.0031, p=0.3420, Supplementary Fig. 4a,b), indicating that basal network activity does not
359 influence the resting vascular tone. By contrast, it dramatically reduced the overall vascular
360 response (-19.6 ± 10.5 %.min, p= 0.04966, Fig. 4a and d1) and the magnitude of evoked
361 vasodilation (6.8 ± 2.4 %.min, p= 0.00844, Fig. 4d2) without altering the maximal dilation (2.2
362 ± 0.6%, p=0.11114, Fig. 4d3) or its time to peak (1256 ± 192 s, p= 0.07716, Fig. 4e2). In
363 addition, the onset and the duration of vasodilation were respectively delayed (1142 ± 210 s,
364 p= 0.00152, Fig. 4e1) and shortened (306 ± 121 s, p= 0.01623, Fig. 4e3). Of note, the
365 vasoconstrictive events were not altered except for their onset and time to peak

366 (Supplementary Fig. 4g1-5). These observations indicate that AP firing is mandatory for the
367 vasodilation induced by 2 Hz photostimulation.
368 We next asked whether NO signaling could be responsible for the vasodilation induced by 2
369 Hz photostimulation. Inhibiting nitric oxide synthases with L-NAME (100 µM (Zonta et al.,
370 2003), n = 9 arterioles) did not alter the arteriolar diameter (diameter before: 15.3 ± 2.1 µm
371 *vs.* after L-NAME: 15.4 ± 2.3 µm, $W_{(9)}$= -2, p=0.9453, Supplementary Fig. 4c,d) indicating that
372 basal NO synthase activity does not influence resting vascular tone. By contrast L-NAME
373 treatment completely abolished the evoked vasodilation as evidenced by its dramatic impact
374 on the overall vascular response (AUC: -71.0 ± 20.4 %.min, p= 0.00042, Fig. 4b and 4d1), as
375 well as on the magnitude (4.9 ± 2.9 %.min, p = 0.00096, Fig. 4d2) and maximal amplitude of
376 vasodilation (1.5 ± 0.9%, p= 0.00172, Fig. 4d3). It also strongly delayed the apparent onset of
377 vasodilation (1407 ± 210 s, p= 0.0004, Fig. 4e1) and reduced its duration (169 ± 100 s,
378 p=0.00059, Fig. 4e3), but not the time to peak (1410 ± 210 s, $H_{(4,54)}$= 8.299, p= 0.08123, Fig.
379 4e2). The overall negative responses observed under NOS inhibition suggest that
380 vasoconstriction was uncovered. Indeed, L-NAME increased the magnitude (-70.1 ± 19.7
381 %.min, p= 0.00234, Supplementary Fig. 4g1) and the maximal amplitude (-8.6 ± 1.9 %, p=
382 0.00089, Supplementary Fig. 4g2) of vasoconstrictive events induced by 2 Hz
383 photostimulation. It also shortened their onset (475 ± 207s, p= 0.01292, Supplementary Fig.
384 4g3) without affecting their time to peak (1056 ± 185 s, p= 0.06502, Supplementary Fig. 4g4)
385 and duration (926 ± 155 s, $H_{(4,54)}$=9.278, p= 0.05452, Supplementary Fig. 4g5). These
386 observations suggest that the vasodilation evoked by 2 Hz photostimulation involves NO
387 synthesis, and that its blockade unmasks vasoconstriction. To confirm that NO signaling is
388 required, we next used ODQ (10 µM (Hepp et al., 2007), n= 12 arterioles) to inhibit the sGC,
389 the intracellular receptor responsible for NO-mediated vasodilation. Similar to NOS
390 inhibition, blockade of NO-signaling did not alter the basal diameter (diameter before: 19.3 ±
391 2.9 µm *vs.* after ODQ: 19.2 ± 2.9 µm, $W_{(12)}$= -14, p=0.6055, Supplementary Fig. 4c,d)
392 confirming that NO signaling does not influence resting vascular tone. Similar to NOS
393 inhibition by L-NAME, ODQ dramatically altered the overall vascular response (-27.6 ± 10.2
394 %.min, p= 0.02253, Fig. 4c and d1) and reduced the magnitude (3.0 ± 1.2%, p=0.00093, Fig.
395 4d2) and maximal amplitude of vasodilation (0.9 ± 0.3 %, p= 0.00172, Fig. 4d3). It also
396 strongly delayed the vasodilation onset (1119 ± 216 s, p= 0.00130, Fig. 4e1), and reduced its
397 duration (147 ± 58 s, p= 0.00123, Fig. 4e3) without impacting the time to peak of

398 vasodilation (1119 ± 216 s, Fig. 4e2). In contrast to L-NAME treatment, ODQ, did not alter
399 the magnitude, amplitude, or kinetic properties of vasoconstrictive events (Supplementary
400 Fig. 4g1-5). Taken together, these results indicate that AP firing is mandatory for the
401 vasodilation evoked by 2 Hz photostimulation, which is mediated by NO synthesis and
402 signaling. Furthermore, they show that 2 Hz optogenetic stimulation induces
403 vasoconstriction that is masked by NO-dependent vasodilation.
404
405 **NPY-induced vasoconstriction involves the Y1 receptor independently of spiking activity.**
406 Since the majority of Sst interneurons are positive for NPY (Fig. 3b1,2) and virtually all
407 cortical type 1 NO-producing interneurons express this neuropeptide (Dawson et al., 1991;
408 Estrada and DeFelipe, 1998; Kubota et al., 1994, 2011; Perrenoud et al., 2012a), NPY could
409 be responsible for the vasoconstriction observed with 20 Hz photostimulation, but also with
410 2 Hz photostimulation under NOS inhibition. We first verified that NPY induced
411 vasoconstriction in a dose-dependent manner (Supplementary Fig. 5). 10 nM NPY (n= 11
412 arterioles) evoked very small vasoconstriction (Supplementary Fig. 5b e1-3), that only
413 differed form control condition (n= 3 arterioles) for their onset (10 nM: 548 ± 194 s, p=
414 0.04430, Supplementary Fig. 5f1). 100 nM (n= 10 arterioles) and 1 µM NPY (n= 9 arterioles)
415 evoked much stronger vasoconstriction, as evidenced by their magnitude (100 nM: -154.9 ±
416 40.7 %.min, p= 0.01154; 1 µM: -162.5 ± 23.0 %.min, p= 0.00474, Supplementary Fig. 5e1),
417 maximal amplitude (100 nM: -13.1 ± 2.2 %, p= 0.02023; 1 µM: -25.1 ± 3.4 %, p= 0.00062,
418 Supplementary Fig. 5e2). Vasoconstriction evoked by 100 nM and 1 µM occurred also much
419 faster (100 nM: 282 ± 43 s, p= 0.04430; 1µM: 147 ± 18 s, p= 0.00281, Supplementary Fig.
420 5e3) and time to peak (100 nM: 545 ± 116 s, p= 0.02912; 1µM: 311 ± 38 s, p= 0.00395,
421 Supplementary Fig. 5e4). They also lasted longer (998 ± 124 s, p= 0.01731; 1µM: 1234 ±
422 104s, p= 0.00113, Supplementary Fig. 5e5). Since the vasoconstriction induced by 20 Hz
423 optogenetic stimulation of Sst-ChR2 and 100 nM NPY were of similar magnitude and
424 maximal amplitude (Fig. 2f2,3 and supplementary Fig. 5e1,2) we next evaluated whether the
425 NPY Y1 antagonist BIBP3226 could abolish the vasoconstriction induced by 100 nM.
426 Pretreatment with BIBP3226 (1µM (Perrenoud et al., 2012b), n= 10 arterioles) dramatically
427 reduced the vasoconstriction induced by 100 nM NPY (Fig. 5a), as evidenced by its effect on
428 the magnitude (-8.0 ± 7.6 %.min, p= 0.00181, Fig. 5c1) and maximum amplitude (-0.8 ± 0.7
429 %, p= 0.00144, Fig. 5c2). BIBP3226 also dramatically delayed the onset (1486 ± 212 s, p=

430 0.01467, Fig. 5c3) and time to peak (1622 ± 137 s, p= 0.00207, Fig. 5c4) of NPY-induced
431 vasoconstriction and reduced its duration (175 ± 148 s, p= 0.01261, Fig. 5c5). These
432 observations confirm that NPY induces strong arteriolar vasoconstriction via Y1 receptors.
433 Since Y1 receptor is expressed by smooth muscle cells (Vanlandewijck et al., 2018; Zhang et
434 al., 2024) but also by neurons (Smith et al., 2019; Tasic et al., 2016; Zeisel et al., 2015) it has
435 been proposed that NPY-induced vasoconstriction could be mediated by intermediary
436 neuronal types (Kaplan et al., 2020). To rule out this possibility we investigated the impact of
437 AP firing inhibition on NPY-induced vasoconstriction. We found that TTX treatment (1 µM,
438 n= 9 arterioles) had no effect on the magnitude (-173.7 ± 58.8 %.min, p= 0.62911, Fig. 5c1),
439 maximum amplitude (-14.3 ± 4.2 %, p= 0.64910, Fig. 5c2), onset (554 ± 239s, p= 0.88537, Fig.
440 5c3), time to peak (752 ± 211 s, p= 0.45002, Fig. 5c4) and duration (903 ± 199s, p= 0.80606,
441 Fig. 2c5) of vasoconstriction induced by 100 nM NPY. Collectively these observations indicate
442 that NPY induces vasoconstriction via the Y1 receptor independently of neuronal activity.
443
444 **Vasoconstriction induced by 20 Hz photostimulation of Sst-ChR2 interneurons requires AP**
445 **firing and NPY Y1 signaling**
446 To investigate the mechanisms responsible for the vasoconstriction induced by 20 Hz
447 optogenetic stimulation of Sst-ChR2 interneurons, we first evaluated the requirement of AP
448 firing. TTX treatment (1µM, n= 10 arterioles) dramatically reduced the magnitude (-14.1 ±
449 5.8, %.min, p= 0.01810, Fig. 6a, c2), maximum amplitude (-1.9 ± 0.5 %, p= 0.00092, Fig. 6c3)
450 of vasoconstriction induced by 20 Hz photostimulation. It also delayed the vasoconstriction
451 onset (990 ± 236 s, p= 0.01993, Fig. 6d1) without significantly altering its apparent time to
452 peak (1163 ± 187 s, Fig. 6d2) and duration (571 ± 196 s, Fig. 6d3). TTX had also no impact on
453 vasodilatory events evoked by 20 Hz photostimulation (Supplementary Fig. 6c1-5). These
454 observations indicate that AP firing is mandatory for vasoconstriction induced by 20 Hz
455 optogenetic stimulation of Sst-ChR2 interneurons. We next investigated whether this
456 vascular response could be mediated by NPY. Antagonizing Y1 receptor in Sst-ChR2 slices
457 with BIBP3226 (1µM, n=10 arterioles) did not alter the arteriolar diameter (diameter before:
458 17.1 ± 2.0 µm *vs.* after BIBP3226: 17.0 ± 2.0 µm, $t_{(9)}$= 0.82945, p= 0.4283, Supplementary Fig.
459 6a,b) indicating that tonic NPY level does not influence resting vascular tone. In contrast,
460 BIBP3226 dramatically reduced the magnitude (-21.8 ± 8.6 %.min, p= 0.01810, Fig. 6a,c2)
461 and the maximum amplitude (-2.0 ± 0.6 %, p= 0.00092, Fig. 6c3) of vasoconstriction induced

462 by 20 Hz optogenetic stimulation. It also delayed the onset of vasoconstriction (934 ± 244 s,
463 p= 0.01993, Fig 6d1) without altering its time to peak (1148 ± 201s, Fig. 6d2) and duration
464 (643 ± 224s, Fig. 6d3). Similar to TTX, BIBP3226 had no impact on the vasodilatory events
465 induced by 20 Hz Photostimulation (Supplementary Fig. 6c1-5). Taken together, these
466 observations indicate that vasoconstriction induced by 20 Hz photostimulation of Sst-ChR2
467 neurons requires both AP firing and NPY signaling through the Y1 receptor.
468
469
470

471 **DISCUSSION**

472 Here we used optogenetics in mouse cortical slices to show that Sst interneurons exert a
473 bimodal vascular response that requires AP firing and whose polarity depends on the
474 stimulation frequency. The vasodilation induced by 2 Hz photostimulation involves NO
475 synthesis and signaling via the sGC, whereas the vasoconstriction induced by 20 Hz
476 photostimulation implies NPY and activation of its Y1 receptor. Consistently, histochemical
477 investigations revealed that subpopulations of photostimulated Sst interneurons express the
478 NOS-1 and/or NPY (Fig. 7).

479

480 **Frequency dependence of the neuronal and vascular responses**

481 The observation that Sst interneurons respond supralinearly to low-frequency optogenetic
482 stimulation is reminiscent of the higher impedance observed at low frequency in
483 hippocampal Sst-positive oriens lacunosum-moleculare cells (Zemankovics et al., 2010),
484 which depends on a high capacitance and a pronounced hyperpolarisation-activated cation
485 current I_h, two features shared by cortical Sst interneurons (Halabisky et al., 2006;
486 Karagiannis et al., 2009, 2021; Perrenoud et al., 2012a). Indeed, according to Ohm's law, a
487 higher impedance at low frequency would have resulted in a larger voltage response
488 induced by the ChR2 photocurrents, resulting in a higher number of spikes per light pulse.
489 We found that depending on the AP firing frequency, Sst interneurons can induce
490 vasodilation or vasoconstriction. These results confirm and extend our previous observations
491 in rat cortical slices showing that the evoked firing of single Sst interneurons at a frequency
492 of at least 8 Hz results in vasoconstriction (Cauli et al., 2004). Similarly, the *in vivo*
493 optogenetic stimulation of GABAergic interneurons was found to induce
494 hyperemia/vasodilation, which can be followed by vasoconstriction (Anenberg et al., 2015;
495 Uhlirova et al., 2016). In addition, photostimulation of Sst interneurons also induced a
496 hyperemic response, followed by a decrease in blood flow that became more pronounced
497 with increasing duration of stimulation (Krawchuk et al., 2019; Lee et al., 2020). Our findings
498 are further supported by the observations showing that the selective optogenetic,
499 chemogenetic or pharmacological stimulation of NOS-1 expressing Sst interneurons induced
500 hyperemia/vasodilation (Echagarruga et al., 2020; Ruff et al., 2024) also support our
501 findings. Nevertheless compared to those *in vivo,* the responses we observed in slices were
502 notably much slower and longer lasting (Krawchuk et al., 2019; Lee et al., 2020). This is likely

503 due to the lower temperature in *ex vivo* experiments which has been reported to slowdown
504 the synthesis of vasoactive messenger (Rancillac et al., 2006) and subsequent reactions. In
505 contrast to *in vivo* observations (Uhlirova et al., 2016; Krawchuk et al., 2019; Lee et al.,
506 2020), the *ex vivo* magnitude of vasoconstriction was greater than that of vasodilation. Here,
507 the absence of vascular tone in slices, which favors vasoconstriction (Blanco et al., 2008),
508 probably led to an underestimation of vasodilation. On the other hand the absence of blood
509 flow in the slices may have reduced the scavenging of NO by hemoglobin (Rancillac et al.,
510 2006), whose *in vivo* concentration locally increases during functional hyperemia (Devor et
511 al., 2007; Lee et al., 2020), thereby prolonging *ex vivo* vasodilation.
512
513 **Cellular and molecular mechanisms of vasodilation and vasoconstriction.**
514 We found that the vasodilation induced by the 2 Hz optogenetic stimulation was dependent
515 on AP firing, NO synthesis and activation of soluble guanylate cyclase (sGC). The mandatory
516 role of APs indicates that Ca^{2+} entry via ChR2 alone is insufficient to drive vasodilation. This
517 likely reflects the essential role of voltage-gated Ca^{2+} channels in somatic Ca^{2+} elevation
518 (Mao et al., 2001) and the subsequent Ca^{2+}-dependent activation of NOS-1, NO release and
519 arteriolar vasodilation (Rancillac et al., 2006; Attwell et al., 2010; Cauli and Hamel, 2010;
520 Mishra et al., 2016; Iadecola, 2017; Cauli and Hamel, 2018). Consistently, some
521 supragranular NOS-1 neurons showed an increase in somatic Ca^{2+} prior to vasodilation
522 evoked by whisker stimulation and/or spontaneous locomotion in awake head-fixed mice
523 whereas others showed a gradual and delayed activation (Ahn et al., 2023). Although type 1
524 NOS-1 interneurons are preferentially located in deep layers (Perrenoud et al., 2012a), our
525 histochemical observations revealed the presence of NOS-1 positive Sst-Cre interneurons in
526 superficial layers. Together with the high excitability of Sst interneurons (Karagiannis et al.,
527 2009, 2021; Perrenoud et al., 2012a), these observations suggest that some of these
528 interneurons correspond to the fast responder NOS-1 neurons (Ahn et al., 2023). The
529 abolition of the optogenetically induced vasodilation evoked by 2 Hz photostimulation by
530 both NOS and sGC inhibition strongly suggests that it is mediated by NO synthesis, release
531 and direct action on smooth muscle cells, leading to their relaxation (Fig. 7). However, NOS
532 inhibition revealed a vasoconstriction, most likely mediated by NPY (Uhlirova et al., 2016),
533 that was not observed when sGC or AP firing was blocked. These observations suggest that a
534 NO-sensitive, but soluble guanylate cyclase-independent, mechanism of vasodilation

535 counterbalanced the vasoconstriction disclosed by L-NAME. Active astrocytes, which have
536 been shown to produce vasodilatory epoxyeicosatrienoic acids via the P450 epoxygenase
537 (Alkayed et al., 1997), may be responsible for such a vasodilation. Indeed, astrocytes have
538 been reported to be robustly activated by the repetitive firing of Sst interneurons (Mariotti
539 et al., 2018), and the P450 expoygenase, which is expressed in arteriolar but not cappillary
540 endfeet (Mishra et al., 2016), is inhibited by NO (Roman, 2002; Metea and Newman, 2006;
541 Attwell et al., 2010).
542 We found that vasoconstriction predominates over vasodilation when Sst-ChR2 interneurons
543 are photostimulated at 20 Hz. This reflects the much higher number of NPY-positive Sst-
544 ChR2 interneurons compared to type 1 NOS-1 interneurons (Karagiannis et al., 2009;
545 Perrenoud et al., 2012a) and the dense network of NPY positive terminals on blood vessels
546 (Abounader and Hamel, 1997). Furthermore, the release of NPY from large dense-core
547 vesicles requires a higher firing frequency than the release of neurotransmitters from
548 synaptic vesicles (Baraban and Tallent, 2004). It is also possible that the release of NO
549 requires a lower firing frequency than that of NPY. We found that optogenetically induced
550 vasoconstriction was almost completely abolished by the antagonism of Y1 receptors,
551 suggesting that this effect was essentially mediated by NPY, as reported for the optogenetic
552 stimulation of GABAergic interneurons (Uhlirova et al., 2016). We cannot exclude the
553 indirect contribution of Sst and GABA which can exert vasoconstrictive effects (Long et al.,
554 1992; Fergus and Lee, 1997). Indeed, the repetitive firing of Sst interneurons robustly
555 activates astrocytes via Sst and $GABA_B$ receptors (Mariotti et al., 2018), which could in turn
556 induce vasoconstriction via 20-hydroxyeicosatetraenoic acid (Mulligan and MacVicar, 2004)
557 and/or K+ (Girouard et al., 2010). However, Sst is not as efficient as NPY in inducing
558 vasoconstriction in cortical slices (Cauli et al., 2004), and the amount of Sst in the cerebral
559 cortex is reduced in Sst-Cre mice (Viollet et al., 2017), but not that of NPY. On the other
560 hand, the vasoconstrictor effect of the $GABA_B$ receptor activation requires AP firing (Fergus
561 and Lee, 1997), suggesting that it is mediated by neurons and not by astrocytes. Thus, it is
562 more likely that the vasoconstriction induced by 20 Hz optogenetic stimulation of Sst-ChR2
563 interneurons is essentially mediated by NPY and the Y1 receptors.
564
565 **Physiological relevance of the bidirectional control of neurovascular coupling by Sst-**
566 **interneurons**

567 The ability of Sst interneurons to drive a bimodal vascular response *ex vivo* depending on
568 firing frequency is consistent with *in vivo* observations showing that increasing the duration
569 and/or the frequency of photostimulation of Sst-ChR2 interneurons favors the observation
570 of decreased blood flow, in addition to hyperemia (Krawchuk et al., 2019; Lee et al., 2020).
571 However, the evoked decrease in blood flow appears to be more pronounced at a site
572 different from the site of hyperemia (Lee et al., 2020). This is reminiscent of the
573 center/surround pattern of vasodilation/vasoconstriction observed *in vivo* in response to
574 sensory stimulation, with the vasodilation in the activated area preceding the peripheral
575 vasoconstriction (Devor et al., 2007; Boorman et al., 2010; Uhlirova et al., 2016). Because
576 fast-responding NOS-1 neurons are activated before the onset of vasodilation (Ahn et al.,
577 2023), they are most likely involved in the initiation of vasodilation. Consistently, local NO
578 production precedes functional hyperemia but disappears before the end of stimulation
579 (Buerk et al., 2003), presumably because of the short half-life of NO (Wood and Garthwaite,
580 1994) and its increased scavenging induced by functional hyperemia. The delayed and/or
581 peripheral vasoconstriction (Devor et al., 2007; Uhlirova et al., 2016; Krawchuk et al., 2019;
582 Lee et al., 2020) could be due to its blunting by early occurring vasodilation, a higher level of
583 activity required for NPY release (Baraban and Tallent, 2004), as suggested by our
584 observations, and/or a different site of action of NO and NPY (Estrada and DeFelipe, 1998).
585 Sst/NOS-1/NPY neurons largely correspond to long-range GABAergic neurons (Tomioka et
586 al., 2005) and have been shown to locally induce vasodilation (Echagarruga et al., 2020; Ruff
587 et al., 2024). It remains to determine whether their interhemispheric long-range projection
588 (Ruff et al., 2024) could explain the vasoconstriction observed contralaterally to the
589 activated area (Devor et al., 2008) when their activity is elevated. Sst/NOS-1/NPY also
590 correspond to cortical sleep active neurons (Gerashchenko et al., 2008; Kilduff et al., 2011).
591 Furthermore, Sst and Sst/NOS-1 interneurons are involved in slow and delta wave activities,
592 respectively (Morairty et al., 2013; Funk et al., 2017; Zielinski et al., 2019), a frequency range
593 associated with sleep that we showed was the most efficient at activating them.
594 Interestingly, oscillating vasodilation of large amplitude and a vasoconstriction are observed
595 during non REM sleep and upon awakening, respectively (Turner et al., 2020; Bojarskaite et
596 al., 2023). Whether the coordinated action of NO and NPY could participate in these
597 hemodynamic changes in a frequency-dependent manner remains also to be determined.
598

599 **Bidirectional control of neurovascular coupling by Sst interneurons in pathological**
600 **conditions**

601 Several neurological disorders, such as epilepsy (Sada et al., 2015; Gaxiola-Valdez et al.,
602 2017) or Alzheimer's disease (Palop et al., 2007; Kimbrough et al., 2015; Le Douce J. et al.,
603 2020), associate hyperactivity with gliovascular and metabolic deficits that are likely to alter
604 the control of neurovascular coupling by Sst interneurons. For example, cerebral lactate,
605 which is produced by astrocytes from glucose during excitatory transmission (Pellerin and
606 Magistretti, 1994; Cauli et al., 2023), is dramatically increased in epilepsy (Slais et al., 2008).
607 Drugs that interfere with lactate metabolism by neurons have emerged as a promising
608 strategy for treating epilepsy (Sada et al., 2015), an effect that involves the neuronal uptake
609 of lactate, its oxidative metabolism and the subsequent closure of ATP-sensitive potassium
610 channels. Since Sst interneurons functionally express these channels (Karagiannis et al.,
611 2021) and are among the neurons showing the highest mitochondrial content (Gulyas et al.,
612 2006), their activity is likely to be efficiently enhanced by the presence of lactate and its
613 oxidative metabolism. This could favor the GABAergic inhibition of pyramidal cells
614 (Silberberg and Markram, 2007), but also decreased glutamatergic transmission (Bacci et al.,
615 2002), and Y1-mediated vasoconstriction (Uhlirova et al., 2016), thereby mitigating lactate-
616 induced hyperactivity (Sada et al., 2015).

617 Hyperactivity has also been reported in several models of Alzheimer's disease (Palop et al.,
618 2007; Bezzina et al., 2015; Zott et al., 2019), and loss of Sst interneurons has been observed
619 in patients (Gaspar et al., 1989) and in the early stages of a mouse model of the disease
620 (Ramos et al., 2006). Furthermore, Sst/NOS-1/NPY interneurons play a key role in non-REM
621 sleep (Gerashchenko et al., 2008; Morairty et al., 2013; Zielinski et al., 2019), during which
622 the fluctuations in the perivascular space favor the clearance of β-amyloid peptides (Iliff et
623 al., 2013; Xie et al., 2013; Bojarskaite et al., 2023). These observations suggest that the
624 control of NVC by Sst interneurons may be altered early, accelerating amyloid plaque
625 accumulation and disease progression. However, NVC has been shown to be impaired (Niwa
626 et al., 2002; Kimbrough et al., 2015; Lourenco et al., 2017), unchanged (Sharp et al., 2020) or
627 even enhanced (Shabir et al., 2020; Kim et al., 2024), making it difficult to assess its
628 alterations. Whether these differences depend on the mouse model, the stage of disease
629 progression, or the experimental condition remains to be investigated.

Conclusion

Here, using a combination of approaches, we describe the mechanisms by which Sst interneurons bidirectionally control NVC as a function of their firing frequency. Vasodilation was preferentially evoked at low-frequency photostimulation and primarily involves NO release and activation of its vascular receptor sGC. In contrast, vasoconstriction was more reliably induced at high frequency and involves NPY release and activation of the vascular receptor Y1. This finding will help to update the interpretation of the functional brain imaging signals used to map network activity in health and disease (Iadecola, 2017; Zhang and Raichle, 2010). This bimodal control of neurovascular coupling may also help to define therapeutic targets for epilepsy and Alzheimer's disease in which hyperactivity, gliovascular and metabolic deficits overlap (Palop and Mucke, 2010; Sada et al., 2015; Gaxiola-Valdez et al., 2017).

Data availability statement

The data that support the results of this study are available from the corresponding author upon reasonable request.

Competing interests

The authors declare no competing interests.

Acknowledgements

We acknowledge the invaluable support of the animal (RongIBPS) and imaging facilities of the IBPS. Financial support was provided by grants from the Agence Nationale de la Recherche (ANR-17-CE37-0010-03, B.C.; ANR-20-CE14-0025, D.L.; ANR-23-CE14-0038-01, B.C.), and the i-Bio initiative of Sorbonne University (B.C.). B.M was supported by a fellowship form Centre National de la Recherche Scientifique. B.L.G. and E.B. were supported by fellowships from Fondation pour la Recherche sur Alzheimer.

Author contributions

B.M., J.O.R, S.P. B.L.G., M.T., and E.B. designed experiments, acquired and analyzed the data, and edited the manuscript. B.M. and B.C. drafted the manuscript. L.R.V.C. edited the manuscript. I.D. designed experiments and edited the manuscript. H.S. analyzed the data.

662 D.L. provided resources and edited the manuscript. B.C. designed experiments, analyzed the
663 data and edited the manuscript.
664
665
666 **REFERENCES**

667 Abounader R, Hamel E. 1997. Associations between neuropeptide Y nerve terminals and
668 intraparenchymal microvessels in rat and human cerebral cortex. *JComp Neurol* **388**:444–
669 453.
670 Ahn SJ, Anfray A, Anrather J, Iadecola C. 2023. Calcium transients in nNOS neurons underlie distinct
671 phases of the neurovascular response to barrel cortex activation in awake mice. *J Cereb*
672 *Blood Flow Metab* **43**:1633–1647. doi:10.1177/0271678X231173175
673 Alkayed NJ, Birks EK, Narayanan J, Petrie KA, Kohler-Cabot AE, Harder DR. 1997. Role of P-450
674 arachidonic acid epoxygenase in the response of cerebral blood flow to glutamate in rats.
675 *Stroke* **28**:1066–1072.
676 Anenberg E, Chan AW, Xie Y, LeDue JM, Murphy TH. 2015. Optogenetic stimulation of GABA neurons
677 can decrease local neuronal activity while increasing cortical blood flow. *JCerebBlood Flow*
678 *Metab*.
679 Ascoli GA, Alonso-Nanclares L, Anderson SA, Barrionuevo G, avides-Piccione R, Burkhalter A, Buzsaki
680 G, Cauli B, DeFelipe J, Fairen A, Feldmeyer D, Fishell G, Fregnac Y, Freund TF, Gardner D,
681 Gardner EP, Goldberg JH, Helmstaedter M, Hestrin S, Karube F, Kisvarday ZF, Lambolez B,
682 Lewis DA, Marin O, Markram H, Munoz A, Packer A, Petersen CC, Rockland KS, Rossier J, Rudy
683 B, Somogyi P, Staiger JF, Tamas G, Thomson AM, Toledo-Rodriguez M, Wang Y, West DC,
684 Yuste R. 2008. Petilla terminology: nomenclature of features of GABAergic interneurons of
685 the cerebral cortex. *NatRevNeurosci* **9**:557–568.
686 Attwell D, Buchan AM, Charpak S, Lauritzen M, MacVicar BA, Newman EA. 2010. Glial and neuronal
687 control of brain blood flow. *Nature* **468**:232–243.
688 Bacci A, Huguenard JR, Prince D a. 2002. Differential modulation of synaptic transmission by
689 neuropeptide Y in rat neocortical neurons. *Proc Natl Acad Sci U S A* **99**:17125–30.
690 doi:10.1073/pnas.012481899
691 Baraban SC, Tallent MK. 2004. Interneuron Diversity series: Interneuronal neuropeptides--
692 endogenous regulators of neuronal excitability. *Trends Neurosci* **27**:135–142.
693 Benjamini Y, Hochberg Y. 1995. Controlling the False Discovery Rate: A Practical and Powerful
694 Approach to Multiple Testing. *J R Stat Soc Ser B Stat Methodol* **57**:289–300.
695 doi:10.1111/j.2517-6161.1995.tb02031.x
696 Bezzina C, Verret L, Juan C, Remaud J, Halley H, Rampon C, Dahan L. 2015. Early Onset of
697 Hypersynchronous Network Activity and Expression of a Marker of Chronic Seizures in the
698 Tg2576 Mouse Model of Alzheimer's Disease. *PLOS ONE* **10**:e0119910.
699 doi:10.1371/journal.pone.0119910
700 Blanco VM, Stern JE, Filosa JA. 2008. Tone-dependent vascular responses to astrocyte-derived
701 signals. *AmJPhysiol Heart CircPhysiol* **294**:H2855–H2863.
702 Bojarskaite L, Vallet A, Bjørnstad DM, Gullestad Binder KM, Cunen C, Heuser K, Kuchta M, Mardal K-
703 A, Enger R. 2023. Sleep cycle-dependent vascular dynamics in male mice and the predicted
704 effects on perivascular cerebrospinal fluid flow and solute transport. *Nat Commun* **14**:953.
705 doi:10.1038/s41467-023-36643-5
706 Boorman L, Kennerley AJ, Johnston D, Jones M, Zheng Y, Redgrave P, Berwick J. 2010. Negative blood
707 oxygen level dependence in the rat: a model for investigating the role of suppression in
708 neurovascular coupling. *JNeurosci* **30**:4285–4294.

709 Buerk DG, Ances BM, Greenberg JH, Detre JA. 2003. Temporal dynamics of brain tissue nitric oxide
710 during functional forepaw stimulation in rats. *Neuroimage* **18**:1–9.
711 Cauli B, Audinat E, Lambolez B, Angulo MC, Ropert N, Tsuzuki K, Hestrin S, Rossier J. 1997. Molecular
712 and physiological diversity of cortical nonpyramidal cells. *JNeurosci* **17**:3894–3906.
713 Cauli B, Dusart I, Li D. 2023. Lactate as a determinant of neuronal excitability, neuroenergetics and
714 beyond. *Neurobiol Dis* **184**:106207. doi:10.1016/j.nbd.2023.106207
715 Cauli B, Hamel E. 2018. Brain Perfusion and Astrocytes. *Trends Neurosci* **41**:409–413.
716 Cauli B, Hamel E. 2010. Revisiting the role of neurons in neurovascular coupling. *Front*
717 *Neuroenergetics* **2**:9.
718 Cauli B, Tong XK, Rancillac A, Serluca N, Lambolez B, Rossier J, Hamel E. 2004. Cortical GABA
719 interneurons in neurovascular coupling: relays for subcortical vasoactive pathways. *JNeurosci*
720 **24**:8940–8949.
721 Choi M, Yoon J, Choi C. 2010. Label-free optical control of arterial contraction. *JBiomedOpt*
722 **15**:015006.
723 Dawson TM, Bredt DS, Fotuhi M, Hwang PM, Snyder SH. 1991. Nitric oxide synthase and neuronal
724 NADPH diaphorase are identical in brain and peripheral tissues. *ProcNatlAcadSciUSA*
725 **88**:7797–7801.
726 DeFelipe J, Lopez-Cruz PL, avides-Piccione R, Bielza C, Larranaga P, Anderson S, Burkhalter A, Cauli B,
727 Fairen A, Feldmeyer D, Fishell G, Fitzpatrick D, Freund TF, Gonzalez-Burgos G, Hestrin S, Hill S,
728 Hof PR, Huang J, Jones EG, Kawaguchi Y, Kisvarday Z, Kubota Y, Lewis DA, Marin O, Markram
729 H, McBain CJ, Meyer HS, Monyer H, Nelson SB, Rockland K, Rossier J, Rubenstein JL, Rudy B,
730 Scanziani M, Shepherd GM, Sherwood CC, Staiger JF, Tamas G, Thomson A, Wang Y, Yuste R,
731 Ascoli GA. 2013. New insights into the classification and nomenclature of cortical GABAergic
732 interneurons. *NatRevNeurosci*. doi:10.1038/nrn3444
733 Devienne G, Le Gac B, Piquet J, Cauli B. 2018. Single Cell Multiplex Reverse Transcription Polymerase
734 Chain Reaction After Patch-clamp. *JVisExp*.
735 Devor A, Hillman EM, Tian P, Waeber C, Teng IC, Ruvinskaya L, Shalinsky MH, Zhu H, Haslinger RH,
736 Narayanan SN, Ulbert I, Dunn AK, Lo EH, Rosen BR, Dale AM, Kleinfeld D, Boas DA. 2008.
737 Stimulus-induced changes in blood flow and 2-deoxyglucose uptake dissociate in ipsilateral
738 somatosensory cortex. *JNeurosci* **28**:14347–14357.
739 Devor A, Tian P, Nishimura N, Teng IC, Hillman EM, Narayanan SN, Ulbert I, Boas DA, Kleinfeld D, Dale
740 AM. 2007. Suppressed neuronal activity and concurrent arteriolar vasoconstriction may
741 explain negative blood oxygenation level-dependent signal. *JNeurosci* **27**:4452–4459.
742 Dodt HU, Zieglgansberger W. 1998. Visualization of neuronal form and function in brain slices by
743 infrared videomicroscopy. *HistochemJ* **30**:141–152.
744 Drew PJ. 2022. Neurovascular coupling: motive unknown. *Trends Neurosci* **45**:809–819.
745 Echagarruga CT, Gheres KW, Norwood JN, Drew PJ. 2020. nNOS-expressing interneurons control
746 basal and behaviorally evoked arterial dilation in somatosensory cortex of mice. *Elife* **9**.
747 Estrada C, DeFelipe J. 1998. Nitric oxide-producing neurons in the neocortex: morphological and
748 functional relationship with intraparenchymal microvasculature. *CerebCortex* **8**:193–203.
749 Fergus A, Lee KS. 1997. GABAergic regulation of cerebral microvascular tone in the rat. *JCerebBlood*
750 *Flow Metab* **17**:992–1003.
751 Funk CM, Peelman K, Bellesi M, Marshall W, Cirelli C, Tononi G. 2017. Role of Somatostatin-Positive
752 Cortical Interneurons in the Generation of Sleep Slow Waves. *JNeurosci* **37**:9132–9148.
753 Gaspar P, Duyckaerts C, Febvret A, Benoit R, Beck B, Berger B. 1989. Subpopulations of somatostatin
754 28-immunoreactive neurons display different vulnerability in senile dementia of the
755 Alzheimer type. *Brain Res* **490**:1–13.
756 Gaxiola-Valdez I, Singh S, Perera T, Sandy S, Li E, Federico P. 2017. Seizure onset zone localization
757 using postictal hypoperfusion detected by arterial spin labelling MRI. *Brain* **140**:2895–2911.
758 Gerashchenko D, Wisor JP, Burns D, Reh RK, Shiromani PJ, Sakurai T, de la I, Kilduff TS. 2008.
759 Identification of a population of sleep-active cerebral cortex neurons. *ProcNatlAcadSciUSA*.

760 Girouard H, Bonev AD, Hannah RM, Meredith A, Aldrich RW, Nelson MT. 2010. Astrocytic endfoot
761 Ca2+ and BK channels determine both arteriolar dilation and constriction.
762 *ProcNatlAcadSciUSA* **107**:3811–3816.
763 Gulyas AI, Buzsaki G, Freund TF, Hirase H. 2006. Populations of hippocampal inhibitory neurons
764 express different levels of cytochrome c. *EurJNeurosci* **23**:2581–2594.
765 Halabisky BE, Shen F, Huguenard JR, Prince DA. 2006. Electrophysiological Classification of
766 Somatostatin-positive Interneurons in Mouse Sensorimotor Cortex. *JNeurophysiol*.
767 Hartmann DA, Berthiaume AA, Grant RI, Harrill SA, Koski T, Tieu T, McDowell KP, Faino AV, Kelly AL,
768 Shih AY. 2021. Brain capillary pericytes exert a substantial but slow influence on blood flow.
769 *NatNeurosci* **24**:633–645.
770 Hendry SH, Jones EG, Emson PC. 1984. Morphology, distribution, and synaptic relations of
771 somatostatin- and neuropeptide Y-immunoreactive neurons in rat and monkey neocortex.
772 *JNeurosci* **4**:2497–2517.
773 Hepp R, Tricoire L, Hu E, Gervasi N, Paupardin-Tritsch D, Lambolez B, Vincent P. 2007.
774 Phosphodiesterase type 2 and the homeostasis of cyclic GMP in living thalamic neurons.
775 *JNeurochem* **102**:1875–1886.
776 Hill RA, Tong L, Yuan P, Murikinati S, Gupta S, Grutzendler J. 2015. Regional Blood Flow in the Normal
777 and Ischemic Brain Is Controlled by Arteriolar Smooth Muscle Cell Contractility and Not by
778 Capillary Pericytes. *Neuron* **87**:95–110.
779 Hu H, Cavendish JZ, Agmon A. 2013. Not all that glitters is gold: off-target recombination in the
780 somatostatin-IRES-Cre mouse line labels a subset of fast-spiking interneurons. *Front Neural*
781 *Circuits* **7**:195.
782 Iadecola C. 2017. The Neurovascular Unit Coming of Age: A Journey through Neurovascular Coupling
783 in Health and Disease. *Neuron* **96**:17–42.
784 Iliff JJ, Wang M, Zeppenfeld DM, Venkataraman A, Plog BA, Liao Y, Deane R, Nedergaard M. 2013.
785 Cerebral Arterial Pulsation Drives Paravascular CSF-Interstitial Fluid Exchange in the Murine
786 Brain. *JNeurosci* **33**:18190–18199.
787 Kaplan L, Chow BW, Gu C. 2020. Neuronal regulation of the blood-brain barrier and neurovascular
788 coupling. *NatRevNeurosci* **21**:416–432.
789 Karagiannis A, Gallopin T, David C, Battaglia D, Geoffroy H, Rossier J, Hillman EM, Staiger JF, Cauli B.
790 2009. Classification of NPY-expressing neocortical interneurons. *JNeurosci* **29**:3642–3659.
791 Karagiannis A, Gallopin T, Lacroix A, Plaisier F, Piquet J, Geoffroy H, Hepp R, Naude J, Le GB, Egger R,
792 Lambolez B, Li D, Rossier J, Staiger JF, Imamura H, Seino S, Roeper J, Cauli B. 2021. Lactate is
793 an energy substrate for rodent cortical neurons and enhances their firing activity. *Elife*
794 **10**:e71424.
795 Kilduff TS, Cauli B, Gerashchenko D. 2011. Activation of cortical interneurons during sleep: an
796 anatomical link to homeostatic sleep regulation? *Trends Neurosci* **34**:10–19.
797 Kim TA, Cruz G, Syty MD, Wang F, Wang X, Duan A, Halterman M, Xiong Q, Palop JJ, Ge S. 2024.
798 Neural circuit mechanisms underlying aberrantly prolonged functional hyperemia in young
799 Alzheimer's disease mice. *Mol Psychiatry*. doi:10.1038/s41380-024-02680-9
800 Kimbrough IF, Robel S, Roberson ED, Sontheimer H. 2015. Vascular amyloidosis impairs the
801 gliovascular unit in a mouse model of Alzheimer's disease. *Brain* **138**:3716–3733.
802 Krawchuk MB, Ruff CF, Yang X, Ross SE, Vazquez AL. 2019. Optogenetic assessment of VIP, PV, SOM
803 and NOS inhibitory neuron activity and cerebral blood flow regulation in mouse somato-
804 sensory cortex 1. *JCerebBlood Flow Metab* 271678X19870105.
805 Krogsgaard A, Sperling L, Dahlqvist M, Thomsen K, Vydmantaite G, Li F, Thunemann M, Lauritzen M,
806 Lind BL. 2023. PV interneurons evoke astrocytic Ca(2+) responses in awake mice, which
807 contributes to neurovascular coupling. *Glia*.
808 Kubota Y, Hattori R, Yui Y. 1994. Three distinct subpopulations of GABAergic neurons in rat frontal
809 agranular cortex. *Brain Res* **649**:159–173.

810 Kubota Y, Shigematsu N, Karube F, Sekigawa A, Kato S, Yamaguchi N, Hirai Y, Morishima M,
811 Kawaguchi Y. 2011. Selective coexpression of multiple chemical markers defines discrete
812 populations of neocortical GABAergic neurons. *CerebCortex* **21**:1803–1817.
813 Lacroix A, Toussay X, Anenberg E, Lecrux C, Ferreirós N, Karagiannis A, Plaisier F, Chausson P, Jarlier F,
814 Burgess SA, Hillman EMC, Tegeder I, Murphy TH, Hamel E, Cauli B. 2015. COX-2-Derived
815 Prostaglandin E2 Produced by Pyramidal Neurons Contributes to Neurovascular Coupling in
816 the Rodent Cerebral Cortex. *J Neurosci Off J Soc Neurosci* **35**:11791–11810.
817 doi:10.1523/JNEUROSCI.0651-15.2015
818 Le Douce J., Maugard M, Veran J, Matos M, Jego P, Vigneron PA, Faivre E, Toussay X, Vandenberghe
819 M, Balbastre Y, Piquet J, Guiot E, Tran NT, Taverna M, Marinesco S, Koyanagi A, Furuya S,
820 Gaudin-Guerif M, Goutal S, Ghettas A, Pruvost A, Bemelmans AP, Gaillard MC, Cambon K,
821 Stimmer L, Sazdovitch V, Duyckaerts C, Knott G, Herard AS, Delzescaux T, Hantraye P,
822 Brouillet E, Cauli B, Oliet SHR, Panatier A, Bonvento G. 2020. Impairment of Glycolysis-
823 Derived l-Serine Production in Astrocytes Contributes to Cognitive Deficits in Alzheimer's
824 Disease. *Cell Metab* **31**:503–517.
825 Lee L, Boorman L, Glendenning E, Christmas C, Sharp P, Redgrave P, Shabir O, Bracci E, Berwick J,
826 Howarth C. 2020. Key Aspects of Neurovascular Control Mediated by Specific Populations of
827 Inhibitory Cortical Interneurons. *CerebCortex* **30**:2452–2464.
828 Lee S, Hjerling-Leffler J, Zagha E, Fishell G, Rudy B. 2010. The largest group of superficial neocortical
829 GABAergic interneurons expresses ionotropic serotonin receptors. *JNeurosci* **30**:16796–
830 16808.
831 Lin JY, Lin MZ, Steinbach P, Tsien RY. 2009. Characterization of engineered channelrhodopsin variants
832 with improved properties and kinetics. *BiophysJ* **96**:1803–1814.
833 Long JB, Rigamonti DD, Dosaka K, Kraimer JM, Martinez-Arizala A. 1992. Somatostatin causes
834 vasoconstriction, reduces blood flow and increases vascular permeability in the rat central
835 nervous system. *JPharmacolExpTher* **260**:1425–1432.
836 Lourenco CF, Ledo A, Barbosa RM, Laranjinha J. 2017. Neurovascular uncoupling in the triple
837 transgenic model of Alzheimer's disease: Impaired cerebral blood flow response to neuronal-
838 derived nitric oxide signaling. *ExpNeurol* **291**:36–43.
839 Lovick TA, Brown LA, Key BJ. 1999. Neurovascular relationships in hippocampal slices: physiological
840 and anatomical studies of mechanisms underlying flow-metabolism coupling in
841 intraparenchymal microvessels. *Neuroscience* **92**:47–60.
842 Madisen L, Garner AR, Shimaoka D, Chuong AS, Klapoetke NC, Li L, van der BA, Niino Y, Egolf L,
843 Monetti C, Gu H, Mills M, Cheng A, Tasic B, Nguyen TN, Sunkin SM, Benucci A, Nagy A,
844 Miyawaki A, Helmchen F, Empson RM, Knopfel T, Boyden ES, Reid RC, Carandini M, Zeng H.
845 2015. Transgenic mice for intersectional targeting of neural sensors and effectors with high
846 specificity and performance. *Neuron* **85**:942–958.
847 Madisen L, Mao T, Koch H, Zhuo JM, Berenyi A, Fujisawa S, Hsu YW, Garcia AJ III, Gu X, Zanella S,
848 Kidney J, Gu H, Mao Y, Hooks BM, Boyden ES, Buzsaki G, Ramirez JM, Jones AR, Svoboda K,
849 Han X, Turner EE, Zeng H. 2012. A toolbox of Cre-dependent optogenetic transgenic mice for
850 light-induced activation and silencing. *NatNeurosci* **15**:793–802. doi:10.1038/nn.3078
851 Mao BQ, Hamzei-Sichani F, Aronov D, Froemke RC, Yuste R. 2001. Dynamics of spontaneous activity
852 in neocortical slices. *Neuron* **32**:883–898.
853 Mariotti L, Losi G, Lia A, Melone M, Chiavegato A, Gomez-Gonzalo M, Sessolo M, Bovetti S, Forli A,
854 Zonta M, Requie LM, Marcon I, Pugliese A, Viollet C, Bettler B, Fellin T, Conti F, Carmignoto G.
855 2018. Interneuron-specific signaling evokes distinctive somatostatin-mediated responses in
856 adult cortical astrocytes. *NatCommun* **9**:82.
857 Metea MR, Newman EA. 2006. Glial cells dilate and constrict blood vessels: a mechanism of
858 neurovascular coupling. *JNeurosci* **26**:2862–2870.
859 Mishra A, Reynolds JP, Chen Y, Gourine AV, Rusakov DA, Attwell D. 2016. Astrocytes mediate
860 neurovascular signaling to capillary pericytes but not to arterioles. *NatNeurosci* **19**:1619–
861 1627.

862 Morairty SR, Dittrich L, Pasumarthi RK, Valladao D, Heiss JE, Gerashchenko D, Kilduff TS. 2013. A role
863 for cortical nNOS/NK1 neurons in coupling homeostatic sleep drive to EEG slow wave activity.
864 *Proc Natl Acad Sci* **110**:20272–20277. doi:10.1073/pnas.1314762110
865 Mulligan SJ, MacVicar BA. 2004. Calcium transients in astrocyte endfeet cause cerebrovascular
866 constrictions. *Nature* **431**:195–199.
867 Niwa K, Kazama K, Younkin SG, Carlson GA, Iadecola C. 2002. Alterations in cerebral blood flow and
868 glucose utilization in mice overexpressing the amyloid precursor protein. *NeurobiolDis* **9**:61–
869 68.
870 Palop JJ, Chin J, Roberson ED, Wang J, Thwin MT, Bien-Ly N, Yoo J, Ho KO, Yu GQ, Kreitzer A,
871 Finkbeiner S, Noebels JL, Mucke L. 2007. Aberrant excitatory neuronal activity and
872 compensatory remodeling of inhibitory hippocampal circuits in mouse models of Alzheimer's
873 disease. *Neuron* **55**:697–711.
874 Palop JJ, Mucke L. 2010. Amyloid-beta-induced neuronal dysfunction in Alzheimer's disease: from
875 synapses toward neural networks. *NatNeurosci* **13**:812–818.
876 Pellerin L, Magistretti PJ. 1994. Glutamate uptake into astrocytes stimulates aerobic glycolysis: a
877 mechanism coupling neuronal activity to glucose utilization. *ProcNatlAcadSciUSA* **91**:10625–
878 9.
879 Perrenoud Q, Geoffroy H, Gauthier B, Rancillac A, Alfonsi F, Kessaris N, Rossier J, Vitalis T, Gallopin T.
880 2012a. Characterization of Type I and Type II nNOS-Expressing Interneurons in the Barrel
881 Cortex of Mouse. *Front Neural Circuits* **6**:36. doi:10.3389/fncir.2012.00036
882 Perrenoud Q, Rossier J, Ferezou I, Geoffroy H, Gallopin T, Vitalis T, Rancillac A. 2012b. Activation of
883 cortical 5-HT(3) receptor-expressing interneurons induces NO mediated vasodilatations and
884 NPY mediated vasoconstrictions. *Front Neural Circuits* **6**:50. doi:10.3389/fncir.2012.00050
885 Price CJ, Cauli B, Kovacs ER, Kulik A, Lambolez B, Shigemoto R, Capogna M. 2005. Neurogliaform
886 neurons form a novel inhibitory network in the hippocampal CA1 area. *JNeurosci* **25**:6775–
887 6786.
888 Ramos B, Baglietto-Vargas D, del Rio JC, Moreno-Gonzalez I, Santa-Maria C, Jimenez S, Caballero C,
889 Lopez-Tellez JF, Khan ZU, Ruano D, Gutierrez A, Vitorica J. 2006. Early neuropathology of
890 somatostatin/NPY GABAergic cells in the hippocampus of a PS1xAPP transgenic model of
891 Alzheimer's disease. *NeurobiolAging* **27**:1658–1672.
892 Rancillac A, Rossier J, Guille M, Tong XK, Geoffroy H, Amatore C, Arbault S, Hamel E, Cauli B. 2006.
893 Glutamatergic Control of Microvascular Tone by Distinct GABA Neurons in the Cerebellum.
894 *JNeurosci* **26**:6997–7006.
895 Roman RJ. 2002. P-450 metabolites of arachidonic acid in the control of cardiovascular function.
896 *Physiol Rev* **82**:131–185.
897 Ruff CF, Juarez AF, Dienel SJ, Rakymzhan A, tamirano-Espinoza A, Couey J, Fukuda M, Watson AM, Su
898 A, Fish KN, Rubio ME, Hooks BM, Ross SE, Vazquez AL. 2024. Long-range inhibitory neurons
899 mediate cortical neurovascular coupling. *Cell Rep* **43**:113970.
900 Rungta RL, Chaigneau E, Osmanski BF, Charpak S. 2018. Vascular Compartmentalization of Functional
901 Hyperemia from the Synapse to the Pia. *Neuron* **99**:362–375.
902 Rungta RL, Osmanski BF, Boido D, Tanter M, Charpak S. 2017. Light controls cerebral blood flow in
903 naive animals. *NatCommun* **8**:14191.
904 Sada N, Lee S, Katsu T, Otsuki T, Inoue T. 2015. Targeting LDH enzymes with a stiripentol analog to
905 treat epilepsy. *Science* **347**:1362–1367. doi:10.1126/science.aaa1299
906 Schaeffer S, Iadecola C. 2021. Revisiting the neurovascular unit. *NatNeurosci* **24**:1198–1209.
907 Shabir O, Sharp P, Rebollar MA, Boorman L, Howarth C, Wharton SB, Francis SE, Berwick J. 2020.
908 Enhanced Cerebral Blood Volume under Normobaric Hyperoxia in the J20-hAPP Mouse
909 Model of Alzheimer's Disease. *SciRep* **10**:7518.
910 Sharp PS, Ameen-Ali KE, Boorman L, Harris S, Wharton S, Howarth C, Shabir O, Redgrave P, Berwick J.
911 2020. Neurovascular coupling preserved in a chronic mouse model of Alzheimer's disease:
912 Methodology is critical. *J Cereb Blood Flow Metab Off J Int Soc Cereb Blood Flow Metab*
913 **40**:2289–2303. doi:10.1177/0271678X19890830

914 Silberberg G, Markram H. 2007. Disynaptic inhibition between neocortical pyramidal cells mediated
915 by Martinotti cells. *Neuron* **53**:735–746.
916 Slais K, Vorisek I, Zoremba N, Homola A, Dmytrenko L, Sykova E. 2008. Brain metabolism and
917 diffusion in the rat cerebral cortex during pilocarpine-induced status epilepticus. *ExpNeurol*
918 **209**:145–154.
919 Smith SJ, Sumbul U, Graybuck LT, Collman F, Seshamani S, Gala R, Gliko O, Elabbady L, Miller JA,
920 Bakken TE, Rossier J, Yao Z, Lein E, Zeng H, Tasic B, Hawrylycz M. 2019. Single-cell
921 transcriptomic evidence for dense intracortical neuropeptide networks. *Elife* **8**.
922 Sun X, Li P, Luo W, Chen S, Feng N, Wang J, Luo Q. 2010. Investigating the effects of
923 dimethylsulfoxide on hemodynamics during cortical spreading depression by combining laser
924 speckle imaging with optical intrinsic signal imaging. *Lasers SurgMed* **42**:649–655.
925 Taniguchi H, He M, Wu P, Kim S, Paik R, Sugino K, Kvitsiani D, Fu Y, Lu J, Lin Y, Miyoshi G, Shima Y,
926 Fishell G, Nelson SB, Huang ZJ. 2011. A resource of Cre driver lines for genetic targeting of
927 GABAergic neurons in cerebral cortex. *Neuron* **71**:995–1013.
928 doi:10.1016/j.neuron.2011.07.026
929 Tasic B, Menon V, Nguyen TN, Kim TK, Jarsky T, Yao Z, Levi B, Gray LT, Sorensen SA, Dolbeare T,
930 Bertagnolli D, Goldy J, Shapovalova N, Parry S, Lee C, Smith K, Bernard A, Madisen L, Sunkin
931 SM, Hawrylycz M, Koch C, Zeng H. 2016. Adult mouse cortical cell taxonomy revealed by
932 single cell transcriptomics. *NatNeurosci* **19**:335–346.
933 Thevenaz P, Ruttimann UE, Unser M. 1998. A pyramid approach to subpixel registration based on
934 intensity. *IEEE TransImage Process* **7**:27–41.
935 Tomioka R, Okamoto K, Furuta T, Fujiyama F, Iwasato T, Yanagawa Y, Obata K, Kaneko T, Tamamaki
936 N. 2005. Demonstration of long-range GABAergic connections distributed throughout the
937 mouse neocortex. *EurJNeurosci* **21**:1587–1600.
938 Tricoire L, Kubota Y, Cauli B. 2013. Cortical NO interneurons: from embryogenesis to functions. *Front*
939 *Neural Circuits* **7**:105.
940 Tricoire L, Pelkey KA, Daw MI, Sousa VH, Miyoshi G, Jeffries B, Cauli B, Fishell G, McBain CJ. 2010.
941 Common origins of hippocampal ivy and nitric oxide synthase expressing neurogliaform cells.
942 *JNeurosci* **30**:2165–2176.
943 Turner KL, Gheres KW, Proctor EA, Drew PJ. 2020. Neurovascular coupling and bilateral connectivity
944 during NREM and REM sleep. *eLife* **9**:e62071. doi:10.7554/eLife.62071
945 Uhlirova H, Kilic K, Tian P, Thunemann M, Desjardins M, Saisan PA, Sakadzic S, Ness TV, Mateo C,
946 Cheng Q, Weldy KL, Razoux F, Vanderberghe M, Cremonesi JA, Ferri CG, Nizar K, Sridhar VB,
947 Steed TC, Abashin M, Fainman Y, Masliah E, Djurovic S, Andreassen O, Silva GA, Boas DA,
948 Kleinfeld D, Buxton RB, Einevoll GT, Dale AM, Devor A. 2016. Cell type specificity of
949 neurovascular coupling in cerebral cortex. *Elife* **5**:e14315.
950 Vanlandewijck M, He L, Mae MA, Andrae J, Ando K, Del GF, Nahar K, Lebouvier T, Lavina B, Gouveia L,
951 Sun Y, Raschperger E, Rasanen M, Zarb Y, Mochizuki N, Keller A, Lendahl U, Betsholtz C. 2018.
952 A molecular atlas of cell types and zonation in the brain vasculature. *Nature* **554**:475–480.
953 Viollet C, Simon A, Tolle V, Labarthe A, Grouselle D, Loe-Mie Y, Simonneau M, Martel G, Epelbaum J.
954 2017. Somatostatin-IRES-Cre Mice: Between Knockout and Wild-Type? *Front*
955 *EndocrinolLausanne* **8**:131.
956 Wood J, Garthwaite J. 1994. Models of the diffusional spread of nitric oxide: implications for neural
957 nitric oxide signalling and its pharmacological properties. *Neuropharmacology* **33**:1235–1244.
958 Xie L, Kang H, Xu Q, Chen MJ, Liao Y, Thiyagarajan M, O'Donnell J, Christensen DJ, Nicholson C, Iliff JJ,
959 Takano T, Deane R, Nedergaard M. 2013. Sleep drives metabolite clearance from the adult
960 brain. *Science* **342**:373–377.
961 Zeisel A, Manchado AB, Codeluppi S, Lonnerberg P, La MG, Jureus A, Marques S, Munguba H, He L,
962 Betsholtz C, Rolny C, Castelo-Branco G, Hjerling-Leffler J, Linnarsson S. 2015. Cell types in the
963 mouse cortex and hippocampus revealed by single-cell RNA-seq. *Science* **347**:1138–1142.

964 Zemankovics R, Kali S, Paulsen O, Freund TF, Hajos N. 2010. Differences in subthreshold resonance of
965 hippocampal pyramidal cells and interneurons: the role of h-current and passive membrane
966 characteristics. *JPhysiol* **588**:2109–2132.
967 Zhang D, Raichle ME. 2010. Disease and the brain's dark energy. *NatRevNeurol* **6**:15–28.
968 Zhang D, Ruan J, Peng S, Li J, Hu X, Zhang Y, Zhang T, Ge Y, Zhu Z, Xiao X, Zhu Y, Li X, Li T, Zhou L, Gao
969 Q, Zheng G, Zhao B, Li X, Zhu Y, Wu J, Li W, Zhao J, Ge WP, Xu T, Jia JM. 2024. Synaptic-like
970 transmission between neural axons and arteriolar smooth muscle cells drives cerebral
971 neurovascular coupling. *NatNeurosci*.
972 Zielinski MR, Atochin DN, McNally JM, McKenna JT, Huang PL, Strecker RE, Gerashchenko D. 2019.
973 Somatostatin+/nNOS+ neurons are involved in delta electroencephalogram activity and
974 cortical-dependent recognition memory. *Sleep* **42**.
975 Zonta M, Angulo MC, Gobbo S, Rosengarten B, Hossmann KA, Pozzan T, Carmignoto G. 2003. Neuron-
976 to-astrocyte signaling is central to the dynamic control of brain microcirculation. *NatNeurosci*
977 **6**:43–50.
978 Zott B, Simon MM, Hong W, Unger F, Chen-Engerer HJ, Frosch MP, Sakmann B, Walsh DM, Konnerth
979 A. 2019. A vicious cycle of beta amyloid-dependent neuronal hyperactivation. *Science*
980 **365**:559–565.
981

982

983 **FIGURE LEGEND**

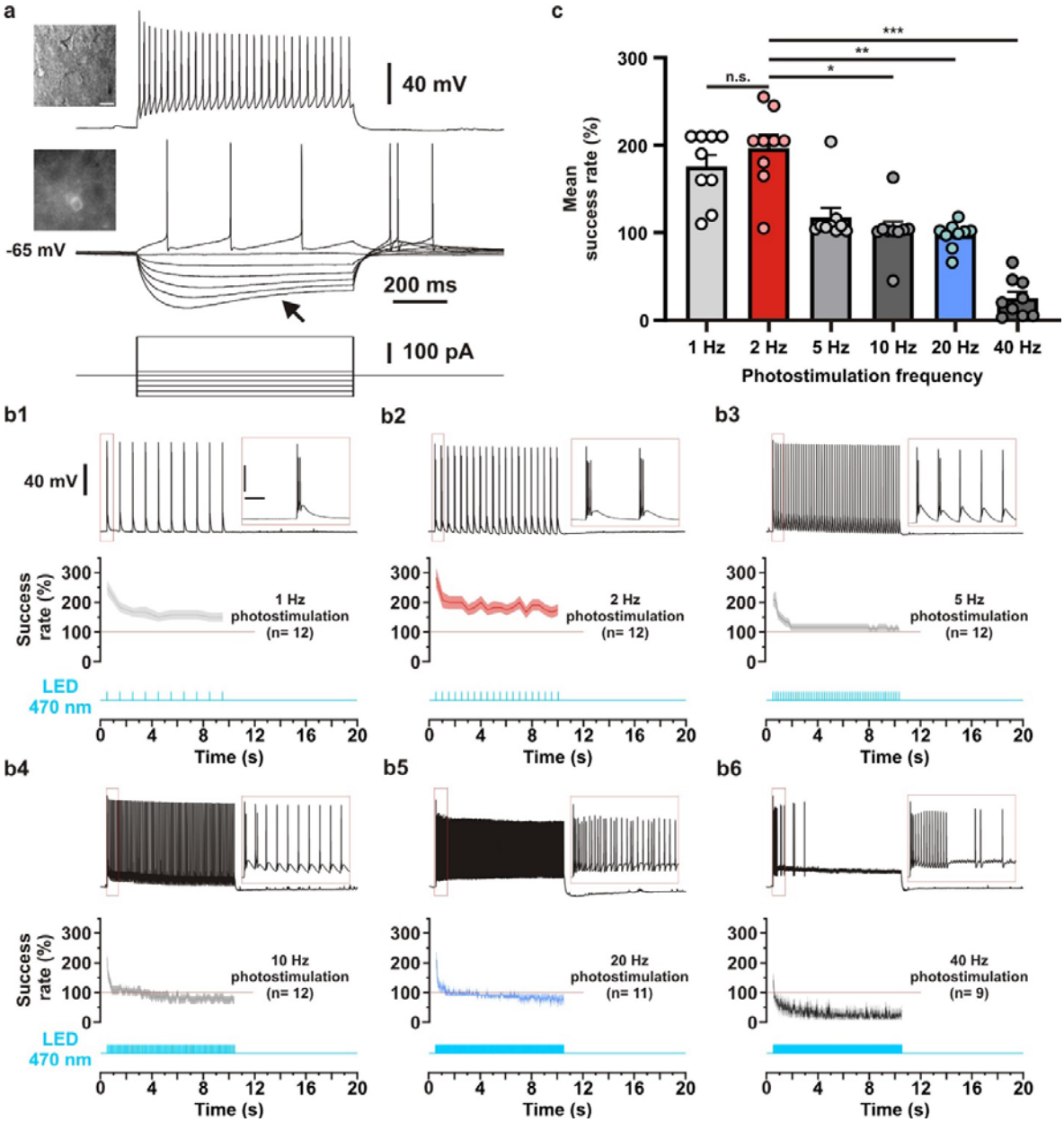

Figure 1: Electrophysiological characterization of cortical Sst-ChR2 neurons. (a) Representative recording showing the voltage responses induced by 800 ms current injections (bottom traces) of -100 pA, -80 pA, -60 pA, -40 pA, -20 pA, 0 pA, +15 and +150 pA in a cortical EYFP/ChR2-expressing neuron from a Sst-Cre:Ai32 mouse. Note the pronounced voltage sag after the initial peak response (arrow) to hyperpolarizing current injections (middle traces). Just-above threshold current pulse (+15 pA) triggered a discharge of three action potentials (middle traces). Note the complex AHP consisting of a fast AHP, a small ADP, and a medium AHP. Near saturation, a strong depolarizing current (+150 pA) elicited a discharge of action potentials with a marked frequency adaptation and a monotonous amplitude accommodation (upper trace). Top inset: IR videomicroscopy picture of the recorded neuron, the pial surface is upward (scale bar, 20 µm). Bottom insets, corresponding field of view showing the EYFP fluorescence of the recorded neuron. **(b1-6)** Voltage responses (upper traces) of the Sst-ChR2 neuron shown in **(a)** induced by photostimulations (470 nm, 10 s train, 5 ms pulses) delivered at 1, 2, 5, 10, 20 and 40 Hz (cyan lower traces) and instantaneous spike success rate (middle trace). The red boxes highlight the first second of the zoomed recording in the right insets

(scaled bars 200 ms, 40 mV). The red lines represent a spike success rate of 100%. Note that more than one action potential is elicited per light pulse delivered at 1 or 2 Hz whereas at frequencies above 5 Hz this success rate rapidly decreases to a maximum of one spike per light pulse. (**c**) Histogram showing the average spike success rate induced by photostimulations at 1, 2, 5, 10, 20, or 40 Hz (n = 9 Sst-ChR2 cortical neurons from 6 SST-Cre:Ai32 mice). Note the average spike success rate exceeding 100 % at photostimulation frequencies lower than 10 Hz. Data are presented as means ± SEM. The SEMs envelope the mean traces Statistically different with *p< 0.05, **p< 0.01 and ***p< 0.001; n.s.: not statistically significant.

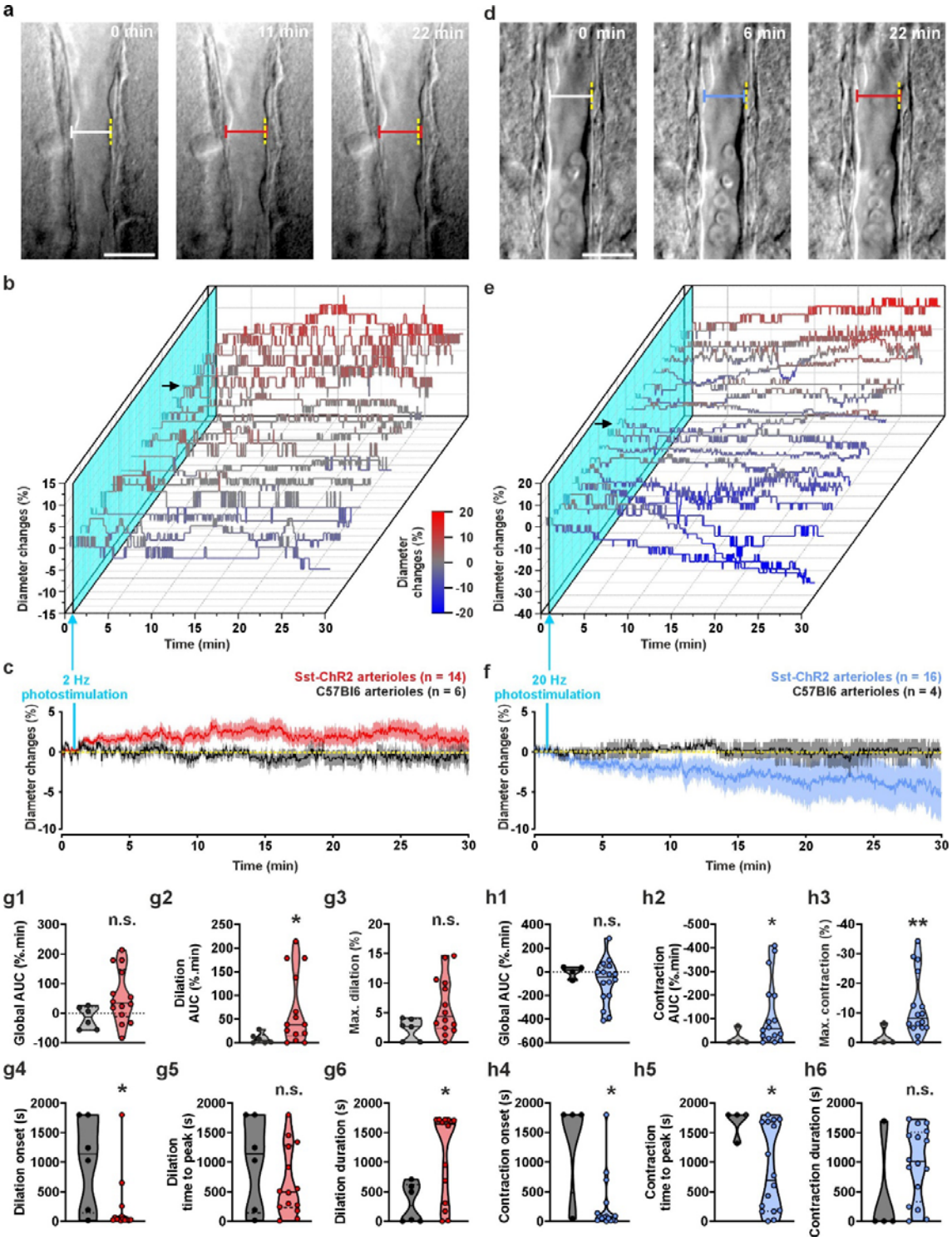

Figure 2: Bidirectional frequency-dependent vascular response induced by optogenetic stimulation of cortical Sst-ChR2 neurons. (a, d) Representative examples of infrared pictures of diving arterioles and diameter measurements before (0 min) and after (6, 11, 22 min) photostimulation at 2 Hz **(a)** and 20 Hz **(d)** in Sst-Cre:Ai32 cortical slices. The pial surface is upward. Scale bars 20 µm. **(a, d)** White, red and blue calipers correspond to baseline, dilated, and contracted arteriolar diameters, respectively. The dashed yellow lines indicate the initial diameters. Note the slight increase **(a)** and decrease followed by an increase **(d)** in diameter induced by photostimulation delivered at 2 Hz **(a)**

1017 and 20 Hz **(d)**, respectively. **(b, e)** Waterfall plots showing the kinetics of changes in diameter of
1018 single arterioles induced by photostimulation at 2 Hz **(b)** and 20 Hz **(e)**. The inset shows the color
1019 code used for constriction (blue) and dilation (red) used in both panels. Arterioles are sorted by
1020 increasing values of total vascular changes. The cyan planes and arrows indicate the onset of
1021 photostimulation. Black arrows indicate changes in diameter of the arterioles shown in **(a)** and **(b)**. **(c,**
1022 **f)** Kinetics of mean diameter changes induced by 2 Hz **(c)** or 20 Hz **(f)** photostimulation. The dashed
1023 yellow lines correspond to the initial diameters. **(c)** Note the average small diameter increase
1024 induced by 2 Hz photostimulation in Sst-Cre:Ai32 (red, n= 14 arterioles from 8 mice) but not in
1025 C57Bl6 arterioles (black, n= 6 arterioles from 5 mice) and **(f)** the average progressive diameter
1026 decrease induced by 20 Hz photostimulation in Sst-Cre:Ai32 (blue, n= 16 arterioles from 10 mice) but
1027 not in WT arterioles (black, n= 4 arterioles from 3 mice). **(g1-6, h1-6)** Violin plots summarizing the
1028 comparison of overall vascular response **(g1, h1)**, magnitude of dilation **(g2)** and contraction **(h2)**,
1029 maximum dilation **(g3)** and contraction **(h3)**, onset **(g4,h4)** time to peak **(g5,h5)** and duration **(g6,h6)**
1030 of dilation **(g2-6)** and contraction **(h2-6)** between arterioles from slices of Sst-Cre:Ai32 and C57Bl6
1031 mice stimulated at 2 **(g1-6**) and 20 Hz **(h1-6)**. Note the larger **(g2),** earlier **(g4)** and longer **(g6)** dilation
1032 in Sst-ChR2 slices stimulated at 2 Hz and the larger **(h2,3)**, and earlier onset **(h4)** and time to peak
1033 **(h5)** contraction in Sst-ChR2 slices stimulated at 20 Hz Data are presented as individual values. Solid
1034 and dashed black bars correspond to median and quartile values. * and ** statistically different from
1035 C57Bl6 mice with $p< 0.05$ and 0.01, respectively. n.s.: not statistically significant.
1036

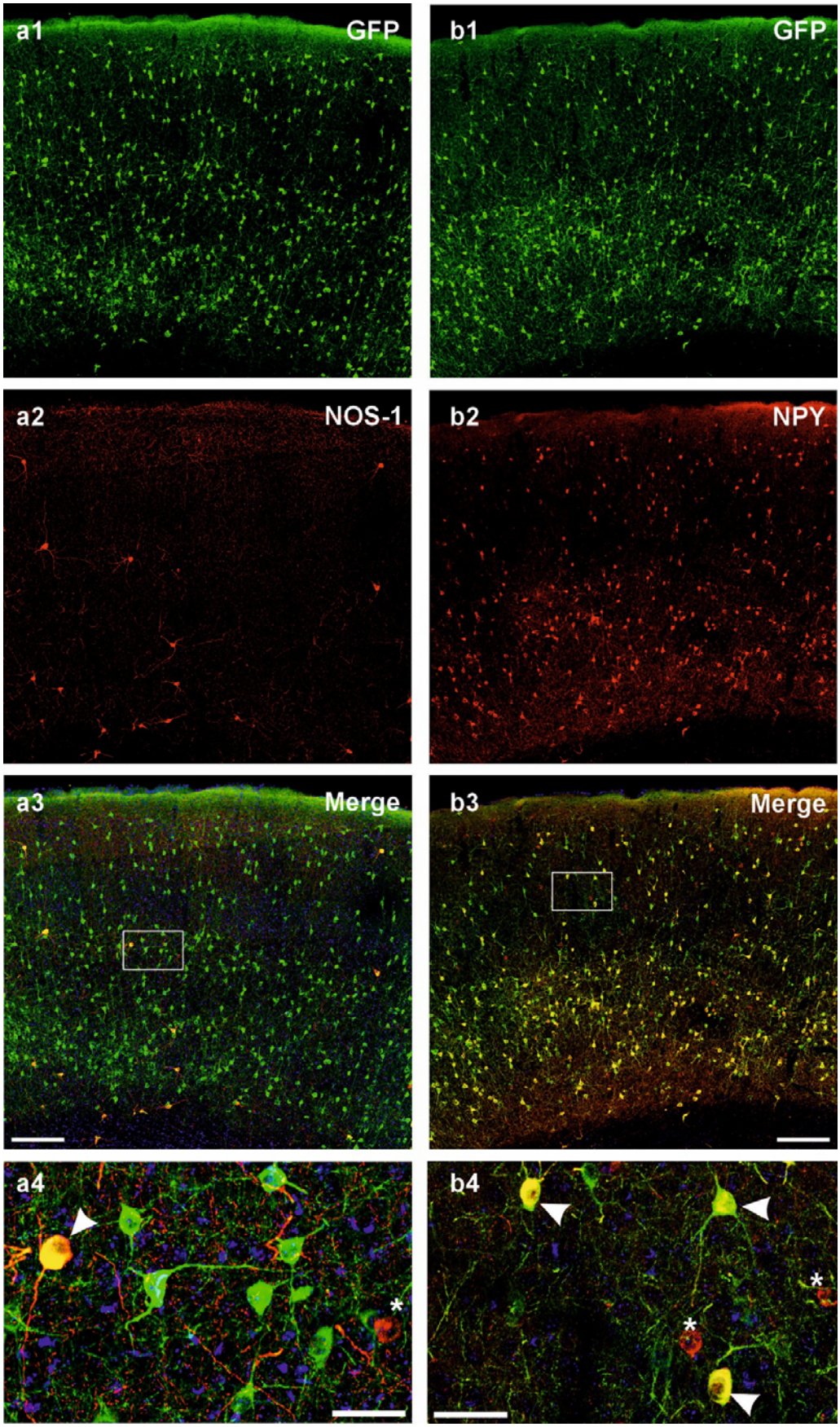

1037

1038 **Figure 3: Expression of NOS-1 and NPY in Sst-Cre neurons. (a1,b1)** Representative maximum
1039 intensity projections of 30 µm thick stacked confocal images showing GFP (green) expression in
1040 cortical slices from Sst-GCaMP6f mice. (**a2**) NOS-1 immunolabeling (red) is present in rare neurons.
1041 (**b2**) Numerous GFP-positive neurons are immunolabeled for NPY (red). (**a3,b3**) Double fluorescence
1042 images showing the co-expression of NOS-1 in rare GFP-positive neurons (a3) and NPY in numerous
1043 GFP positive neurons (b3). The white rectangles in **a3** and **b3** correspond to the zoomed regions
1044 shown in **a4** and **b4**, respectively. Arrowheads indicate GPF-positive neurons immunolabelled for
1045 NOS-1 (**a4**) or NPY (**b4**). Asterisks denote GFP-negative neurons immunostained for NOS-1 (**a4**) or
1046 NPY (**b4**). Scale bars: 200 µm (**a3, b3**) and 40 µm (**a4,b4**).
1047
1048

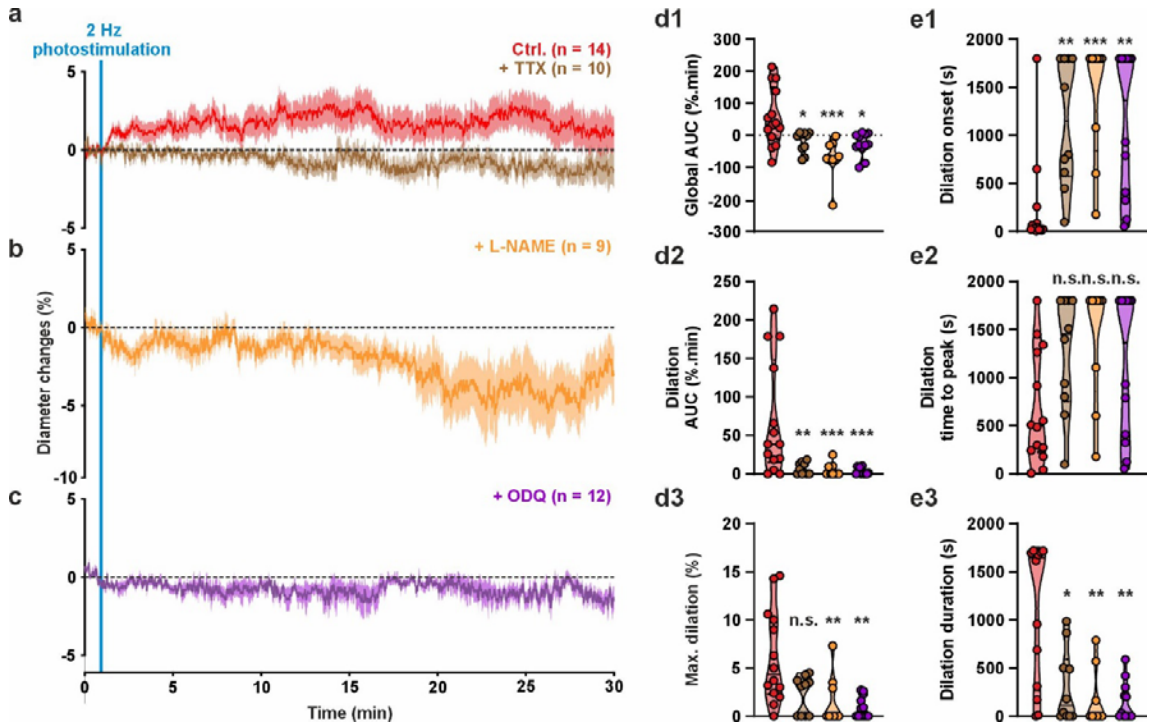

1049 **Figure 4: Vasodilation induced by 2 Hz photostimulation of Sst-ChR2 neurons requires spiking**
1050 **activity and nitric oxide signaling**. **(a, b, c)** Effects of tetrodotoxin (TTX, 1 µM, brown, n= 10 arterioles
1051 from 6 mice), NOS inhibitor (L-NAME, orange, 100 µM, n= 9 arterioles from 6 mice) and ODQ (10 µM,
1052 purple, n= 12 arterioles from 7 mice), on the kinetics of the vascular response induced by 2 Hz
1053 photostimulation of Sst-ChR2 neurons. The red traces correspond to the control condition shown in
1054 Fig. 2b. The SEMs envelope the mean traces. Vasodilation is abolished by blocking action potentials
1055 with TTX **(a)**, inhibiting nitric oxide synthase with L-NAME **(b)** or sGC with ODQ **(c)**. The dashed black
1056 lines indicate the normalized initial diameters. Violin plots summarizing the effects of TTX (brown), L-
1057 NAME (orange) and ODQ (purple) on the overall vascular response **(d1**, $H_{(5,51)}$= 16.105, p= 0.00288**)**,
1058 magnitude **(d2**, $H_{(5,51)}$= 18.625, p= 0.00093**),** maximum **(d3**, $H_{(5,51)}$= 14.834, p=0.00506**)**, onset **(e1**,
1059 $H_{(5,51)}$= 20.592, p= 0.00038**),** time to peak **(e2**, $H_{(5,51)}$= 8.299, p= 0.08123**)**, and duration **(e3**, $H_{(5,51)}$=
1060 16.867, p= 0.00205**)** of vasodilation induced by 2 Hz photostimulation (red). Data are presented as
1061 individual values. Solid and dashed black bars correspond to median and quartile values. * and **
1062 statistically different from control condition with p<0.05 and 0.01 respectively.
1063

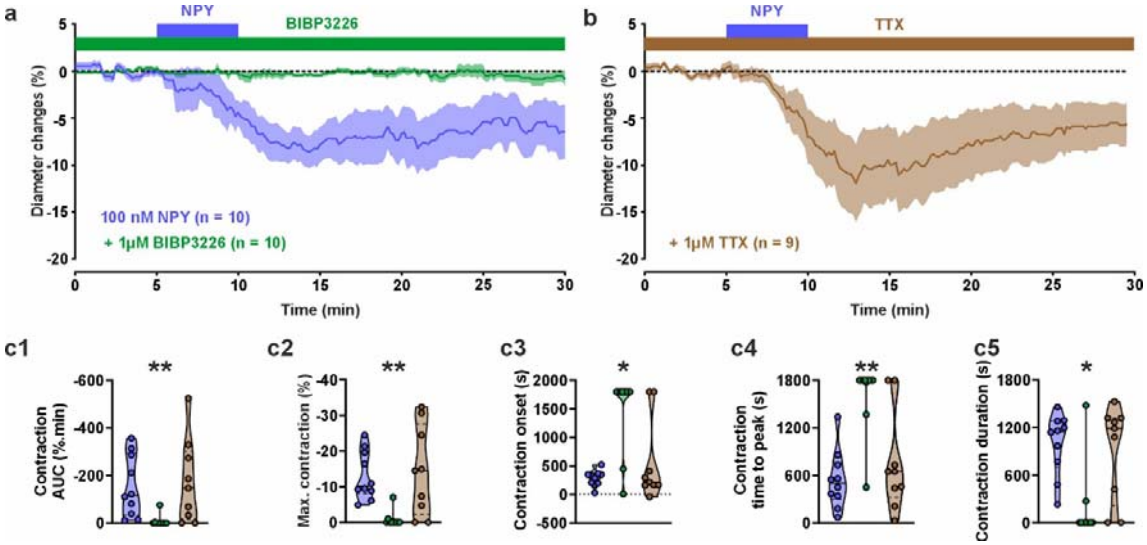

Figure 5: NPY-induced vasoconstriction involves the Y1 receptor independently of spiking activity. (a,b) Kinetics of diameter changes induced by 5 minutes exogenous application of 100 nM NPY (blue bars) under control condition (**a**, blue trace) and in presence of 1 µM BIBP3226 (**a**, green trace, n= 10 arterioles from 6 mice) or 1 µM TTX (**b**, brown trace, n= 9 arterioles from 4 mice). The SEMs envelope the mean traces. Violin plots summarizing the effects of BIBP 3226 (green) and TTX (brown) on the on the magnitude **(c1**, $H_{(4,32)}$= 17.244, p= 0.00063**),** maximum **(c2**, $H_{(4,32)}$= 17.859, p= 0.00047**)**, onset **(c3**, $H_{(4,32)}$= 13.529, p= 0.00362**),** time to peak **(c4**, $H_{(4,32)}$= 16.209, p= 0.00103**)**, and duration **(c5**, $H_{(4,32)}$= 13.557, p= 0.00357**)** of vasoconstriction induced by NPY. The selective NPY Y1 receptor antagonist BIBP3226 but not TTX abolished the NPY-induced vasoconstriction. Data are presented as individual values. Solid and dashed black bars correspond to median and quartile values. * and ** statistically different from the 100 nM control condition with p< 0.05 and 0.01, respectively.

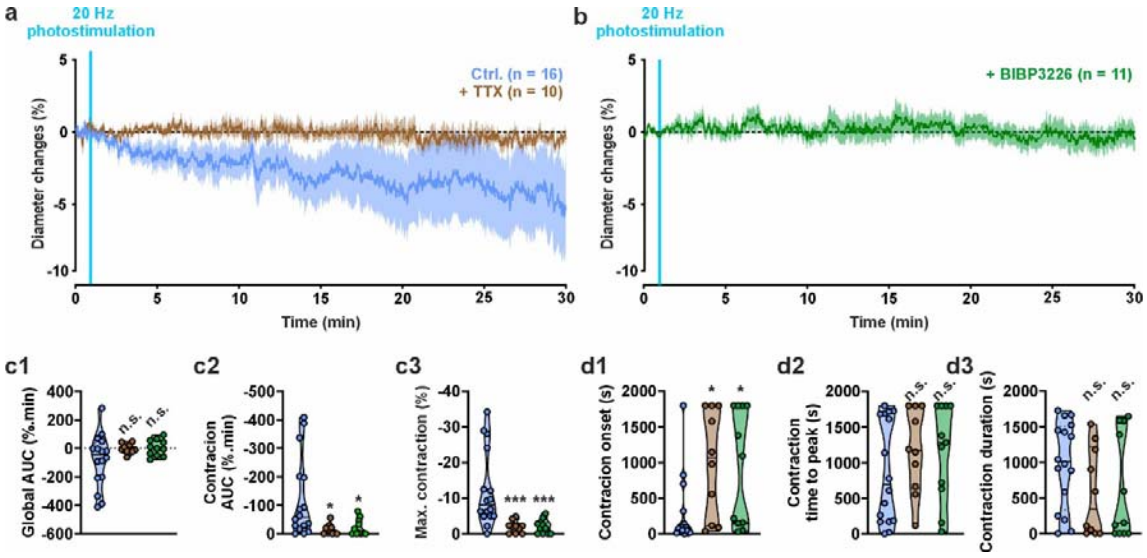

Figure 6: Vasoconstriction induced by 20 Hz photostimulation of Sst-ChR2 neurons requires spiking activity and NPY signaling. (a, b) Effects of tetrodotoxin (TTX, 1 µM, brown, n= 10 arterioles from 5 mice) and the selective Y1 receptor antagonist (BIBP 3226, 1 µM, green, n= 11 arterioles from 9 mice)

on the kinetics of the vascular response induced by 20 Hz photostimulation of Sst-ChR2 neurons. The blue trace corresponds to the control condition shown in Fig. 2e. The SEMs envelope the mean traces. Vasoconstriction is abolished by blocking action potentials with TTX **(a)** or by the selective antagonist of Y1 receptor, BIBP 3226 **(b)**. Violin plots summarizing the effects of TTX (brown) and BIBP 3226 (green) on the overall vascular response **(c1**, $F^*_{(3,22.04)}$= 2.557, p= 0.08117**)**, magnitude **(c2**, $H_{(4,41)}$= 10.774, p= 0.01301**)**, maximum **(c3**, $H_{(4,41)}$= 19.152, p= 0.00025**)**, onset **(d1**, $H_{(4,41)}$= 10.671, p= 0.01364**)**, time to peak **(d2**, $H_{(4,41)}$= 6.373, p= 0.09481**)**, and duration **(d3**, $H_{(4,41)}$= 4.726, p= 0.19300**)** of vasoconstriction induced by 20 Hz photostimulation (cyan). Data are presented as individual values. Solid and dashed black bars correspond to median and quartile values. *, ** and *** statistically different from control condition with p<0.05, p<0,01 and 0.001 respectively.

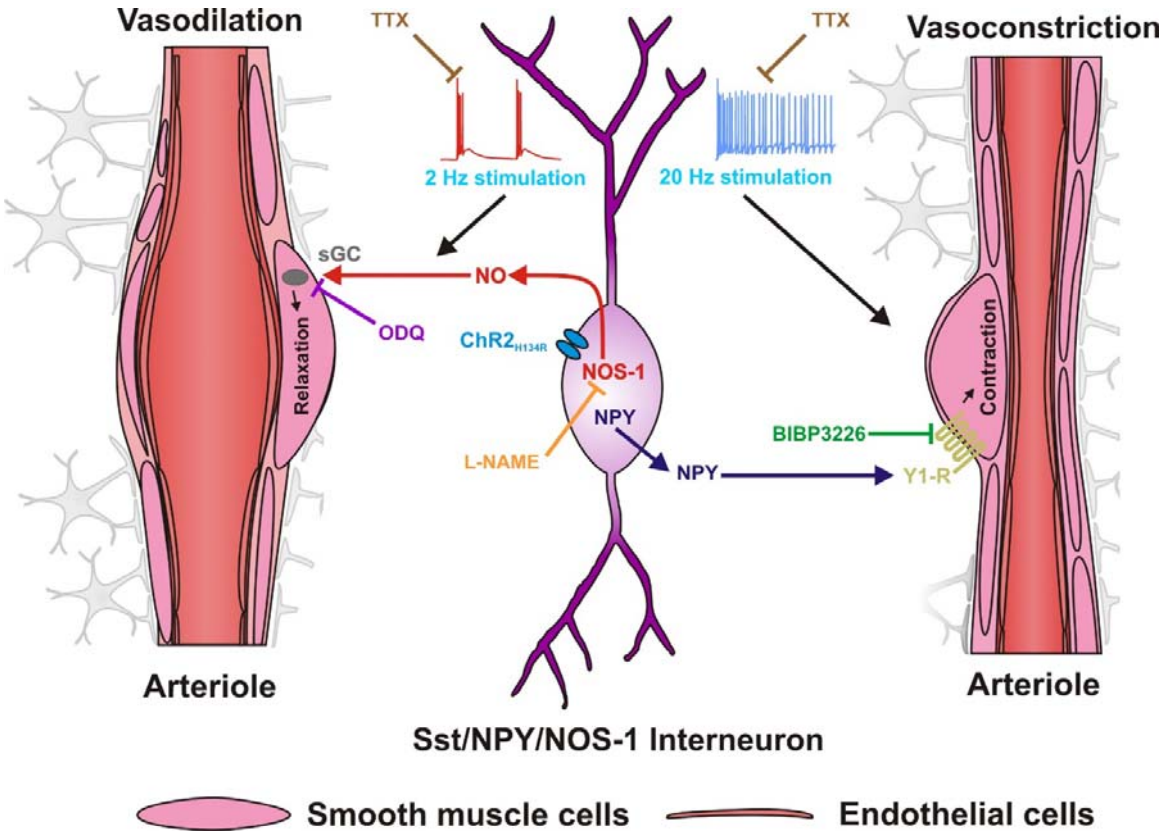

Figure 7: Schematic representation of the mechanisms of bidirectional control of neurovascular coupling by Sst-ChR2 interneurons. Bidirectional responses are shown on both sides of the Sst-NPY-NOS-1 interneuron. **Left:** 2 Hz stimulation of Sst-ChR2 interneurons activates NOS-1 and releases NO which in turn activates the sGC of smooth muscle cells leading to their relaxation and vasodilation. This effect is abolished by TTX (brown) and by inhibition of NOS with L-NAME (orange) and sGC with ODQ (purple). **Right**: 20 Hz photostimulation of Sst-ChR2 interneurons induces NPY release and activation of vascular receptor Y1 leading to smooth muscle cell contraction and vasoconstriction. This effect is suppressed by the TTX (brown) and the Y1 receptor antagonist, BIPB3226 (green).

1101